Experimental validation of a rate-dependent Data-Driven stress Identification method

Adrien Vinel, Rian Seghir, Julien Berthe, Gerald Portemont, Julien Réthoré

Received: Added at production | Revised: Added at production | Accepted: Added at production

DOI: xxx/xxxx

FULL PAPER

Experimental validation of a rate-dependent Data-Driven stress Identification method

Adrien Vinel[1,2] | Rian Seghir[1] | Julien Berthe[2] | Gérald Portemont[2] | Julien Réthoré[1]

[1]GeM, Centrale Nantes, UMR 6183 CNRS, Nantes, France
[2]DMAS, ONERA, F-59014 Lille, France

Correspondence
Adrien Vinel, GeM, Centrale Nantes, France. Email: adrien.vinel@ec-nantes.fr

Abstract

Document de travail

KEYWORDS:

1 | INTRODUCTION

Recently, several strategies have been adopted to estimate stress fields in non-standard experiments without using a constitutive law. These strategies all rely on full-field measurements and a regularization of the ill-posed mechanical problem, but differ on the chosen regularization.

In 2014, Pierron and his co-authors [29] devised a strategy to estimate stress fields in dynamics without using a constitutive law. To this effect, the strategy relies on the use of a statically determined configuration (an inertial impact test for instance). Under the assumptions of plane stress, and a homogeneous and constant density of the material, the authors are able to estimate the mean stress field profile in the specimen. For this strategy, the acceleration acquired experimentally acts as a load cell, which requires recording kinematic fields at ultra-high speed ($\geq$ 1M fps). This work opened the way to the so called Image-Based Inertial Impact Tests (IBII). Among other, it allowed the authors to identify the elastic modulus and tensile strength of tungsten carbide cermets [9] and a composite [11] at high strain-rate. More recently, the strategy was also applied in a new experimental configuration: the Image-Based Inertial Release (IBIR) test [10]. This new configuration allowed the identification of both quasi-static and high strain-rate elastic modulus and Poisson's ratio for PMMA. In these examples, the boundary conditions (purely inertial test and uniaxial) regularize the problem. If the test is not uniaxial any more, the authors proposed an elegant solution in the case of elastic orthotropic material [28].

Even more recently, in 2021, Liu *et al.* [25] and Cameron and his co-author [3] devised another strategy to estimate stress fields without postulating a constitutive equation. Assuming that the material is isotropic, the methods developed by these authors rely on the alignment of the principal directions of stress with strain or strain-rate. This assumption then allows obtaining a mathematically closed problem, and thus the analytical estimation of stresses. These methods have been tested on numerical example and experimentally in [25]. In [3], the authors discuss the range of validity of such an assumption: mainly in isotropic elasticity, plasticity with associative flow rules and for associative flow rules with an isotropic yield function. Furthermore, this method cannot address the problem of elasto-plastic transition where stresses are not aligned with strains anymore and not aligned with plastic strain-rates yet.

The recent developments in computer science and in particular in the data science field, has lead to the emergence of a third kind of strategy relying on data in the past 4 years: the so called Data-Driven approaches. These methods can be used to either solve the direct problem [15] or the inverse mechanical problem [23]. The so called Data-Driven methods were first introduced in the context of computational mechanics by Kirchdoerfer and Ortiz [15, 16]. In their work, the authors replaced the constitutive equation by a minimization process and a material database. A solution is found by minimizing a distance (which they defined) between computed mechanical states (strains and stresses) and a set of admissible material states. The authors then extended their methods to dynamics [17]. These methods called Data-Driven Computational Mechanics are used to solve the direct problem: find the response of structure (strains and stresses) using a set of

admissible material states, which have to be found experimentally. These works were then derived in order to formulate inverse Data-Driven approaches. Hence, in their work Leygue and his co-authors [23, 24] formulated the inverse problem associated to the Data-Driven Computational Mechanics. This new problem aims to estimate stress fields from heterogeneous experiments without having to explicit any constitutive equation. Using synthetic data, the authors demonstrated the ability of their algorithm to estimate admissible stresses in a structure for various loading cases (quasi-static and dynamic problems) as well as different material behaviours (hyperelasticity, elasto-plastiticy). This Data-Driven method was then applied to experimental data by Dalémat *et al.* in [6]. In this study, perforated hyperelastic membranes are submitted to uniaxial tensile tests. In addition, in a recent paper [5] extensively discuss the proper way to handle imperfect experimental data. The authors especially discuss the boundary conditions for imperfectly defined edges and the way to tackle the issue of missing data. More recently, the Data-Driven strategy was applied by Langlois and his co-authors to experiments on history dependent materials [**?**]. The use of this method enabled them to estimate stress fields for an elasto-platic material that is subjected to the formation of Piobert-Lüders bands. In these strategies, the regularization comes from the assumption that the material response lies on a manifold in a constitutive space which remains to be determined. The underlying hypothesis of this method will be presented later-on in this paper. Furthermore, one could imagine combining this method with the IBII method in order to estimate heterogeneous 2D stress fields in dynamics without needing load measurements.

These emergent strategies can potentially help to assess, without making any assumptions, the validity of material constitutive equations outside their validity domain (*e.g.* heterogeneous tests, with multi-axiality, couplings...). In that context, the Data-Driven Identification formulation and resolution strategy for visco-elasto-plastic materials will first be recalled. Then, a digital twin is built to investigate the ability of such a method to estimate stress fields, and especially its accuracy. At last but not least, the DDI is then applied to data obtained during a high speed tensile test performed on a heterogeneous sample made in steel.

2 | DATA-DRIVEN IDENTIFICATION METHOD

The inverse Data-Driven Identification method requires both, a rich database of displacement fields (obtained for example with DIC on complex sample geometries), and net external forces (usually obtained with a load cell). Combined with conservation laws (balance of linear and angular momentum), valid whatever the material, it is possible to build a minimization problem where the components of stress fields are the sougth parameters. The following section guide the reader up to final formulation of the global minimization problem.

To make the implementation clearer, we use in the following only matrix notation instead of tensorial one. By default, we use $[\bullet]$ for matrices and $\{\bullet\}$ for vectors. When indices are explicitly required they are emphasized as followed, X_i^j, where i and j are matrix rows and columns respectively. Some non-trivial operators are detailed in appendix 28b.

While the main ingredients are recalled in detail we refer interested readers to [23] where the *DDI* problem was originally introduced. This work is also inspired by the works of Eggersmann and his co-authors [7] where the framework was extended for history dependent materials. Furthermore, the modified strategy, regarding the initialization of the problem, proposed in [24] is adopted. Some notations that will be recalled and used in this work was introduced by Langlois and his co-authors in [19]. The problem is formulated here in small strain, however it has already been implemented and used in finite strain in [6, 30]. Moreover, for experimental concerns, we will focus only on plane-stress formalism.

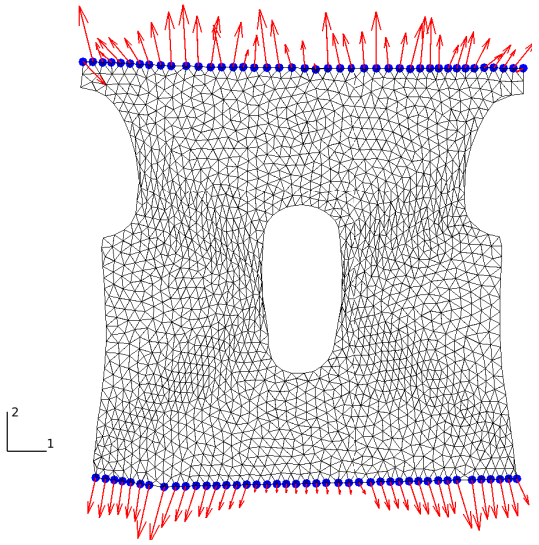

FIGURE 1 2D deformable structure made of T3P1 elements over a domaine Ω. Blue bullets define the border ∂F where loads and / or displacements are prescribed. Red arrows shows a distribution of reaction forces.

2.1 | Static equilibrium problem

The general problem considers a 2D structure made of a deformable material (see Fig. 1). This structure is discretized using a Finite Element mesh with N_e elements and N_n nodes and the loading is discretized though N_t time steps.

Available Data are the following:

- $[u]$: a $2N_n \times N_t$ matrix collecting nodal displacements obtained from DIC over the domaine Ω. The dimension $2N_n$ means that displacement vectors are organized in vector format such as $\left\{u^t\right\} = \left\{u1_1^t, ..., u1_n^t, u2_1^t, ..., u2_n^t\right\}$ where u1 and u2 are transverse and axial displacements respectively (see Fig. 1),

- $[B]$: a $3N_e \times 2N_n$ matrix obtained from the assembly of elementary FEM gradient operators. The dimension $3N_e$ encloses the 3 components of the displacement gradient (see **??** for details). It is computed using the geometry, mesh connectivity and relies on triangular elements and classical linear Lagrange shape functions. It allows for computing strain tensors at every quadrature points, here element centroid noted e. They are collected in a $3N_e \times N_t$ matrix

$$[\varepsilon] = [B]\,[u]\,, \tag{1}$$

- $[w]$: a $3N_e \times 3N_e$ diagonal matrix collecting the elementary integration weights times Jacobian determinants of the transformation of each element from its reference coordinates frame to its actual shape in the global coordinate system,

- $\{F\}$: a N_t vector collecting the net force, along the axial direction 2 (see Fig. 1) of the nodal forces on the boundary ∂F

$$\{F\} = h \sum_{k \in \partial f} f^t_{N_n+k} \quad \forall t \in [1, N_t] \tag{2}$$

with h the thickness of the structure, supposed to be constant, and $[f]$ a $2N_n \times N_t$ matrix collecting the nodal internal forces. $N_n + k$ refers to axial displacements only (see **??** for vector organization)

Static equilibrium can therefore be expressed through a set of N_t systems of $2N_n$ linear equations:

$$\begin{aligned} &[B]^{\mathrm{T}}\,[w]^{\mathrm{T}}\left\{\boldsymbol{\sigma}^t\right\} = \left\{f^t\right\},\ \forall t \in [1, N_t] \\ &\text{with} \sum_{k \in \partial f} f^t_{N_n+k} = \frac{F^t}{h} \text{ and } f^t_k = 0,\ \forall k \in \Omega \backslash \partial F. \end{aligned} \tag{3}$$

Considering boundary conditions, especially the fact that only the net force along the axial direction 2 (see Fig. 1) is usually known in practice, and that displacements are prescribed everywhere else on ∂F, the set of $2N_n$ equations can be reduced to $\hat{N} = 2N_n - 4\,\mathrm{card}(\partial F) + 1$. It is implemented by discarding from the system of equation 3 constrained boundary nodes and by adding the linear combination introduced in Eq. 2. It leads to the definition of news operators $\left[\hat{B}\right]$ and $\left[\hat{f}\right]$ summarizing mechanical equilibrium into a compact form:

$$\left[\hat{B}\right]^{\mathrm{T}}[w]^{\mathrm{T}}\left\{\boldsymbol{\sigma}^t\right\} = \left\{\hat{f}^t\right\},\ \forall t \in [1, N_t]. \tag{4}$$

2.2 | Data-Driven Identification problem

The main idea behind the *DDI* method consists in assuming that a constitutive equation exists, hence there is a constitutive space (still to be defined) where the whole set of mechanical states lies on a manifold. In short, among the infinity of solution of the static problem (see Eq. 4), one seeks for the one that minimizes the spread around an unknown manifold within a well defined constitutive space. Notice that in the following, such a manifold will be approximated by discrete points named material states, in the sense that they literally sample the material response in the constitutive space. Such a discretization allows for regularizing the ill-posed problem of stress identification as we will see later-on.

As a consequence 3 main ingredients have to be defined: (1) such a "well defined" constitutive space, (2) a norm for estimating distances between states in this constitutive space, and (3) the sampling of the manifold. Main assumptions of the method are enclosed in these three ingredients.

Constitutive space has to be chosen wisely regarding the various dependencies of the material response to observable and sought quantities. Following Eggersman *et al.* recommendations [7], the history and time-dependent behaviour of the material will be described using strain, stress and their first order time derivatives. To this effect, similarly to what is done in [19], an incremental approach will be used, leading to a dependence of the current stress to the current strain as well as the former strain and stress.

$$\boldsymbol{\sigma}^t = \hat{\sigma}^t\left(\boldsymbol{\varepsilon}^t, \boldsymbol{\varepsilon}^{t-1}, \boldsymbol{\sigma}^{t-1}\right) \tag{5}$$

$\hat{\sigma}^t$ will be further used as the *DDI* estimation of the actual stress in this particular space. As a result, the constitutive space that will be considered in this work is $\left(\boldsymbol{\varepsilon}^t, \boldsymbol{\varepsilon}^{t-1}, \boldsymbol{\sigma}^t, \boldsymbol{\sigma}^{t-1}\right)$. From a modelling point-of-view, such a differential constitutive space approaches the material response similarly to rate-dependent plasticity models, classically used in high-strain rate simulation like Johnson-Cook models [], which has to be distinguished from visco-plastic models where relaxation time, meaning larger time non-locality, can properly be

taken into account.

Then, let us define a distance in a generic strain and stress related constitutive space. Following [15] we choose a norm built from a symmetric positive definite fourth-order tensor $\mathbb{C}_o$. Noting for example $\{\mathcal{P}^t\}$ and $\{\mathcal{Q}^t\}$, two vectors related to some strain and stress quantities at time t respectively in Voigt notation, an energetic $\|\|^2_{\mathbb{C}_o}$ norm can be introduced as follows:

$$\|\mathcal{P}^t, \mathcal{Q}^t\|^2_{\mathbb{C}_o} = \{\mathcal{P}^t\}^{\mathrm{T}} [\mathbb{C}_o] \{\mathcal{P}^t\} + \{\mathcal{Q}^t\}^{\mathrm{T}} [\mathbb{C}_o] \{\mathcal{Q}^t\}. \quad (6)$$

Normalizing data, such as:

$$\begin{aligned} \{\underline{\mathcal{P}}^t\} &= \left[\sqrt{\mathbb{C}_o}\right] \{\mathcal{P}^t\}, \\ \left\{\underline{\mathcal{Q}}^t\right\} &= \left[\sqrt{\mathbb{C}_o}\right]^{-1} \{\mathcal{Q}^t\}, \end{aligned} \quad (7)$$

the norm simply becomes:

$$\|\mathcal{P}^t, \mathcal{Q}^t\|^2_{\mathbb{C}_o} = \{\underline{\mathcal{P}}^t\}^{\mathrm{T}} \{\underline{\mathcal{P}}^t\} + \left\{\underline{\mathcal{Q}}^t\right\}^{\mathrm{T}} \left\{\underline{\mathcal{Q}}^t\right\}. \quad (8)$$

Notice that the square root of the tensor $\left[\mathbb{C}_o\right]$ is computed using an Eigen decomposition, $\left[\sqrt{\mathbb{C}_o}\right] = [V]\left[\sqrt{D}\right][V]^{\mathrm{T}}$, where $[V]$ and $[D]$ are matrices containing Eigen vectors and values respectively. Such a normalization will help the clustering part of the problem (see Sec. 2.4).

As introduced above, to address the issue of ill-posness of the stress-field identification problem (infinite dimension of the manifold) the material response is discretized with a finite N^* set of unknown material states $(\{\boldsymbol{\varepsilon}^*\}, \{\boldsymbol{\varepsilon}^{**}\}, \{\boldsymbol{\sigma}^*\}, \{\boldsymbol{\sigma}^{**}\})$, where $\bullet^*$ are related to the current state and $\bullet^{**}$ to the former state. We will see that these N^* states are in practice defined as barycenters of mechanical states clusters. These clusters regroup the set of strains and sought stresses $\left(\{\boldsymbol{\varepsilon}^t\}, \{\boldsymbol{\varepsilon}^{t-1}\}, \{\boldsymbol{\sigma}^t\}, \{\boldsymbol{\sigma}^{t-1}\}\right)$ that are close in the $\|\|^2_{\mathbb{C}_o}$ norm sense. The following form of the *DDI* method can therefore be seen as a zero-order approach in the sense that the regularization introduced by the material states is piece-wise constant.

Using the constitutive space introduced in 5, the norm introduced in 8 and the sampling of the material response into N^* current and former states, the problem can be formulated as a global minimization:

$$\min_{\substack{\boldsymbol{\varepsilon}^*\boldsymbol{\varepsilon}^{**}\hat{\boldsymbol{\sigma}} \\ \boldsymbol{\sigma}^*\boldsymbol{\sigma}^{**}S}} \Psi(\boldsymbol{\varepsilon}, \boldsymbol{\varepsilon}^*, \boldsymbol{\varepsilon}^{**}, \hat{\boldsymbol{\sigma}}, \boldsymbol{\sigma}^*, \boldsymbol{\sigma}^{**}, S), \quad (9)$$

where

$$\Psi = \frac{1}{2} \sum_{t=2}^{N_t} \left(\|\mathcal{P}^t, \mathcal{Q}^t\|^2_{\mathbb{C}_o} + \|\mathcal{P}^{t-1}, \mathcal{Q}^{t-1}\|^2_{\mathbb{C}_o} \right), \quad (10)$$

with

$$\begin{aligned} \underline{\mathcal{P}}^t &= \left[\sqrt{p^t}\right] \left(\{\underline{\boldsymbol{\varepsilon}}^t\} - [S^t] \{\underline{\boldsymbol{\varepsilon}}^*\}\right), \\ \underline{\mathcal{P}}^{t-1} &= \left[\sqrt{p^{t-1}}\right] \left(\{\underline{\boldsymbol{\varepsilon}}^{t-1}\} - [S^t] \{\underline{\boldsymbol{\varepsilon}}^{**}\}\right), \\ \underline{\mathcal{Q}}^t &= \left[\sqrt{p^t}\right] \left(\{\underline{\hat{\boldsymbol{\sigma}}}^t\} - [S^t] \{\underline{\boldsymbol{\sigma}}^*\}\right), \\ \underline{\mathcal{Q}}^{t-1} &= \left[\sqrt{p^{t-1}}\right] \left(\{\underline{\hat{\boldsymbol{\sigma}}}^{t-1}\} - [S^t] \{\underline{\boldsymbol{\sigma}}^{**}\}\right), \end{aligned} \quad (11)$$

under the constraint that the equilibrium conditions (Eq. 4) are satisfied. $[p]$ is a $3N_e \times 3N_e \times N_t$ matrix weighing mechanical states contributions for every time-steps within the functional Ψ. A specific section (see Sec. 2.5) is dedicated later-on to address the specific role of these weights in the time and space integral. $[S]$ is a $3N_e \times 3N^* \times N_t$ selection matrix that maps the N^* material states to the mechanical states for every time-steps. Eq. 9 must be understood as the global minimization (time and space) of the scattering of mechanical states around their associated N^* material states (piece-wise barycenters) in the particular constitutive space $(\boldsymbol{\varepsilon}^t, \boldsymbol{\varepsilon}^{t-1}, \boldsymbol{\sigma}^t, \boldsymbol{\sigma}^{t-1})$.

If equilibrium constraints are enforced using Lagrange multipliers, the following cost function can be obtained:

$$\Phi = \Psi + \sum_{t=1}^{N_t} \left(\left[\underline{\hat{B}}\right]^{\mathrm{T}} [w]^{\mathrm{T}} \{\underline{\hat{\boldsymbol{\sigma}}}^t\} - \{\hat{f}^t\} \right) \{\lambda^t\} \quad \forall t \in [1, N_t]. \quad (12)$$

Notice that the introduction of normalized quantities "$\underline{\bullet}$" also requires the normalization of $\underline{\hat{B}}$. It is simply done by assembling normalized gradient operators. Finally, two problems can be formulated: (1) the mechanical and (2) the material one.

The stationarity of Φ with respect to $\{\lambda^t\}$ and $\{\underline{\hat{\sigma}}^t\}$ leads to the mechanical problem and the following set of N_t systems of $3N_e \times \hat{N}$ equations:

$$\begin{bmatrix} \left[\underline{\hat{B}}\right]^{\mathrm{T}} [w]^{\mathrm{T}} & 0 \\ \alpha^t & \left[p^t\right]^{-1} [w] \left[\underline{\hat{B}}\right] \end{bmatrix} \begin{Bmatrix} \underline{\hat{\boldsymbol{\sigma}}}^t \\ \lambda^t \end{Bmatrix} = \begin{Bmatrix} \hat{f}^t \\ D^t \end{Bmatrix} \quad (13)$$

with,

$$\alpha^t = \begin{cases} 1 & \forall t \in [1, N_t], \\ 2 & \forall t \in [2 : N_{t-1}], \end{cases}$$

$$\{D^t\} = \begin{cases} \left[S^{t+1}\right] \{\underline{\boldsymbol{\sigma}}^{**}\} & t = 1, \\ \left[S^{t+1}\right] \{\underline{\boldsymbol{\sigma}}^{**}\} + \left[S^t\right] \{\underline{\boldsymbol{\sigma}}^*\} & \forall t \in [2 : N_{t-1}], \\ \left[S^t\right] \{\underline{\boldsymbol{\sigma}}^*\} & t = N_t. \end{cases} \quad (14)$$

One key element to obtain such an expression is to observe the following relations:

Then, the stationarity with respect to the material states leads to the material problem and the following 4 sets of $3N^*$ equations:

$$\begin{cases} \sum_{t=2}^{N_t} \left[\mathcal{M}^{*t}\right]\left[S^t\right]\left\{\underline{\boldsymbol{\varepsilon}}^*\right\} &= \sum_{t=2}^{N_t} \left[\mathcal{M}^{*t}\right]\left\{\underline{\boldsymbol{\varepsilon}}^t\right\}, \\ \sum_{t=2}^{N_t} \left[\mathcal{M}^{*t}\right]\left[S^t\right]\left\{\underline{\boldsymbol{\sigma}}^*\right\} &= \sum_{t=2}^{N_t} \left[\mathcal{M}^{*t}\right]\left\{\underline{\hat{\boldsymbol{\sigma}}}^t\right\}, \\ \sum_{t=1}^{N_{t-1}} \left[\mathcal{M}^{**t}\right]\left[S^{t+1}\right]\left\{\underline{\boldsymbol{\varepsilon}}^{**}\right\} &= \sum_{t=1}^{N_{t-1}} \left[\mathcal{M}^{**t}\right]\left\{\underline{\boldsymbol{\varepsilon}}^t\right\}, \\ \sum_{t=1}^{N_{t-1}} \left[\mathcal{M}^{**t}\right]\left[S^{t+1}\right]\left\{\underline{\boldsymbol{\sigma}}^{**}\right\} &= \sum_{t=1}^{N_{t-1}} \left[\mathcal{M}^{**t}\right]\left\{\underline{\hat{\boldsymbol{\sigma}}}^t\right\}, \end{cases} \tag{15}$$

with,

$$\begin{aligned} \left[\mathcal{M}^{*t}\right] &= \left[S^t\right]^{\mathrm{T}}\left[p^t\right], \\ \left[\mathcal{M}^{**t}\right] &= \left[S^{t+1}\right]^{\mathrm{T}}\left[p^t\right]. \end{aligned} \tag{16}$$

Stationary with respect to $\left[S^t\right]$, to update the state mapping, is difficult to explicit. Indeed, contrary to other variables, which are continuous numbers of $\mathbb{R}$, $[S]$ is made of discrete numbers of $\mathbb{N}$. As a consequence a brute force method is employed. Detailed are given in Sec. 2.4.

The resolution of such a problem has already been discussed in [24, 36]. It relies on a staggered algorithm that computes alternatively the Lagrangian multipliers and the correction of the stress fields for a given material state set and selection matrices (called the mechanical problem), then the update of the material states set and selection matrices for given stresses (called the material problem). These two steps are discussed in the next sections.

2.3 | Resolution of the mechanical problem

Let us consider a given set of material states $\left(\left\{\underline{\boldsymbol{\varepsilon}}^*\right\},\left\{\underline{\boldsymbol{\varepsilon}}^{**}\right\},\left\{\underline{\boldsymbol{\sigma}}^*\right\},\left\{\underline{\boldsymbol{\sigma}}^{**}\right\}\right)$ and a given mapping through the selection matrix $[S]$.

They can be initialized using experimental strains, a first guess for the stress fields and basic K-means algorithm. In the present case, an FE simulation with imposed experimental loads is first performed using an arbitrary elasto-plastic model (see Sec. 28b). An elastic initialization could also be used but would necessarily increase the number of iterations and potentially converge to local minima. Initializing the problem with a model also provide a root for improving it since it eventually allows for emphasizing areas, in the constitutive space, where *DDI* deviates from the model giving clues for its improvement.

The mechanical problem can be solved by substitution, leading first to the computation of the Lagrangian multipliers:

$$\underbrace{\left[\hat{\underline{\boldsymbol{B}}}\right]^{\mathrm{T}}[w]^{\mathrm{T}}\left[p^t\right]^{-1}[w]\left[\hat{\underline{\boldsymbol{B}}}\right]}_{[\mathcal{M}^t]}\left\{\lambda^t\right\} = \underbrace{\left[\hat{\underline{\boldsymbol{B}}}\right]^{\mathrm{T}}[w]^{\mathrm{T}}\left\{D^t\right\} - \alpha^t\left\{\hat{f}^t\right\}}_{\{b^t\}} \quad \forall t \in [1, N_t]. \tag{17}$$

It consists in a set of N_t systems of $\hat{N}$ independent linear equations to solve. This is done using a Cholesky decomposition:

Finally, stresses are updated using the second line of the system of equations 13.

$$\left\{\hat{\underline{\boldsymbol{\sigma}}}^t\right\} = \frac{1}{\alpha^t}\left(\left\{D^t\right\} - \left[p^t\right]^{-1}[w]\left[\hat{\underline{\boldsymbol{B}}}\right]\left\{\lambda^t\right\}\right), \forall t \in [1, N_t]. \tag{18}$$

2.4 | Resolution of the material problem

First, the mapping operator, i.e. $[S]$, must be computed for given stress fields and the actual set of material states. As mentioned above this is done in a brute force way, finding for each element e the material state N_i^* that is the closest with respect to $\|\|^2_{\mathbb{C}_o}$. This is relatively expensive as it requires, for each mechanical state, to compute its distance to all material states in the material database. This operation is the bottleneck of the method.

Once this matrix obtained, the set of material states $\left(\left\{\underline{\boldsymbol{\varepsilon}}^*\right\},\left\{\underline{\boldsymbol{\varepsilon}}^{**}\right\},\left\{\underline{\boldsymbol{\sigma}}^*\right\},\left\{\underline{\boldsymbol{\sigma}}^{**}\right\}\right)$ is actualized using Eq. 15. The complexity of the resolution mainly depends on the form of $\left[p^t\right]$. If $\left[p^t\right]$ is diagonal, as it has always been the case in the literature according the author knowledge, the resolution of Eq. 15 simply consists in computing $5 \times 3N^*$ independent averages or weighted averages of the mechanical states in elements assigned to each material states through $[S]$.

For example current and former material strains are found such as:

$$
\begin{aligned}
\underline{\boldsymbol{\varepsilon}}_i^{*} &= \frac{\sum_{t=2}^{N_t}\sum_{j=1}^{3N_e}\left(\mathcal{S}_j^i\right)^t\left(p_j^k\right)^t\underline{\boldsymbol{\varepsilon}}_k^t}{\sum_{t=2}^{N_t}\sum_{k=1}^{3N_e}\sum_{j=1}^{3N_e}\left(\mathcal{S}_j^i\right)^t\left(p_j^k\right)^t\left(\mathcal{S}_k^l\right)^t} \\
\underline{\boldsymbol{\varepsilon}}_i^{**} &= \frac{\sum_{t=1}^{N_t-1}\sum_{j=1}^{3N_e}\left(\mathcal{S}_j^i\right)^{t+1}\left(p_j^k\right)^t\underline{\boldsymbol{\varepsilon}}_k^t}{\sum_{t=1}^{N_t-1}\sum_{k=1}^{3N_e}\sum_{j=1}^{3N_e}\left(\mathcal{S}_j^i\right)^{t+1}\left(p_j^k\right)^t\left(\mathcal{S}_k^l\right)^{t+1}} \\
&\qquad\qquad \forall i \in [1:3N^*]
\end{aligned}
\tag{19}
$$

The next section discusses the choice of such diagonal $\left[p^t\right]$.

2.5 | Choice of a Weighing matrix

The weighing matrix of the elementary distance between one mechanical state to its corresponding material state $[p]$, introduced in the *DDI* norm (see Eq. 8), can be wisely used as a natural filter for noisy experimental inputs. Input of the *DDI* being itself an output of the DIC inverse problem, it is necessarily biased and corrupted by noise. Finding a way to mitigate this issue is crucial for the application of the *DDI* method in real life experiments. Some solutions have already been proposed in the literature for such a weighting matrix.

Evenif it has not been explicitly written as such in literature, two cases can be found: (1) $\left[p^t\right] = \mathbf{I}_2$, the identity matrix [], and (2) $\left[p^t\right] = [w]$. The first solution gives an equal weight to every elements, strain components and time-steps. The authors found it useful when the objective is to identify stresses in vicinity of a localization band using a refined mesh hence where the sought information is localized in space and time. Indeed, the second option, classical for FE integrals, gives more weight to large and undistorted elements discarding data arising from spatial localization.

In this study another route will be explored. A numerical twin of the considered experiment will be constructed (see Section 4). This allows to have access to the solution sought by the DDI. Thus, for each time steps, one can know the error (w.r.t. the stresses) for each element. Similarly to what is done when using the Virtual Fields Method and the [], from this numerical twin a weight can be given for each element at each time step. This weight will be defined using the relative stress relative error: the lower the relative error, the more confident one can be in the results given by the considered element at the considered time step and thus the closer to one the weight. This will be further described in Subsection **??**.

2.6 | Schematic of the global minimization problem

To summarize, the resolution of the global minimization problem, *i.e.* computing $\left(\left\{\underline{\boldsymbol{\varepsilon}}^*\right\},\left\{\underline{\boldsymbol{\varepsilon}}^{**}\right\},\left\{\underline{\boldsymbol{\sigma}}^*\right\},\left\{\underline{\boldsymbol{\sigma}}^{**}\right\}\right)$, $\left[\underline{\hat{\boldsymbol{\sigma}}}\right]$ and $[\mathcal{S}]$, is performed using the following staggered algorithm [19]:

1. initialize $[\hat{\boldsymbol{\sigma}}]$ using a FE simulation with a arbitrary model
2. normalize input dataset to get $\left(\left[\underline{\hat{\boldsymbol{\sigma}}}\right],\left[\underline{\boldsymbol{\varepsilon}}\right]\right)$
3. initialize $\left(\left\{\underline{\boldsymbol{\varepsilon}}^*\right\},\left\{\underline{\boldsymbol{\varepsilon}}^{**}\right\},\left\{\underline{\boldsymbol{\sigma}}^*\right\},\left\{\underline{\boldsymbol{\sigma}}^{**}\right\}\right)$ and $[\mathcal{S}]$ using a k-means algorithm [26] on $\left(\left\{\underline{\boldsymbol{\varepsilon}}^t\right\},\left\{\underline{\boldsymbol{\varepsilon}}^{t-1}\right\},\left\{\underline{\hat{\boldsymbol{\sigma}}}^t\right\},\left\{\underline{\hat{\boldsymbol{\sigma}}}^{t-1}\right\}\right)\forall t \in [1, N_t]$,
4. solve the mechanical problem (see Sec. 2.3),
5. solve the material problem (see Sec. 2.4),
6. iterate step 5 until convergence of $[\mathcal{S}]$. It usually takes less than 3 iterations to converge
7. iterate steps 4 through 5 until convergence of $[\mathcal{S}]$ and $\left[\underline{\hat{\boldsymbol{\sigma}}}\right]$. One iteration from step 4 to 5 will be called a cycle.

2.7 | Parameters of the method

Once the framework of the *DDI* method fixed, meaning that a particular constitutive space (see Eq. 5) and a particular norm (see Eq. 8) are selected, 5 parameters remain to be adjusted by the user and will affect performances of the algorithm.

- the number of material states N^* sampling the material response
- the amplitude and the exact form of $\mathbb{C}_o$ within the norm
- the two convergence criteria
- and the Weighing matrix of mechanical states $[p]$

The first one and part of the second one has already been investigated by Dalémat and her co-authors in [5]. They compared the stresses of FE simulations, considered as the reference, to the one obtained using the *DDI* with different number of material states values. They concluded that a small number of material states leads to an insufficient sampling of the strain-stress manifolds, and thus, to significant error. A high number of material states also leads to significant error, since it will give more weight to outliers and increase the sensitivity to noise (similarly to the overfitting phenomenon for regressions). In their work, the authors recommend a number of material states so that $20 \leq \frac{(N_t-1)\cdot N_e}{N^*} \leq 100$. The influence of the magnitude of $\mathbb{C}_o$ was found to be straightforward. Indeed, Eq. 7 shows that by choosing a tensor with

high values, the normalization will give more weight to strains compared to stresses. So it may be relevant to use high amplitude to give more weight to strains which are obtained experimentally, compared to stresses which are unknowns and change during the method.

While the influence of the magnitude of $\mathbb{C}_o$ is straightforward, the influence of the symmetry class of the tensor remains unknown. In the present work, the fourth-order tensor that will be used is a Hooke tensor for an isotropic material, hence its definition will only be dependent of the choice of a pseudo-Young modulus E_o (the magnitude) and a pseudo-Poisson ratio ν_o. Nevertheless, it seems reasonable to assume that the use of a pseudo isotropic elastic tensor would not necessarily lead to a satisfying clustering, for instance, of anisotropic mechanical states. However, to the author knowledge, the question of the influence of the symmetry class of $\mathbb{C}_o$ has not yet be investigated and it is not the objective of the present work.

Regarding the two convergence criteria needed for resolution, this work proposes the following expressions:

- for the material problem criterion, we use the convergence rate of the data-driven distance Ψ (see Eq. 9) at each each iteration i. That is to say:
$$\frac{|\Psi_i - \Psi_{i-1}|}{\Psi_0} \geq \epsilon_{mat} \tag{20}$$
where Ψ_0 is its initial value and ϵ_{mat} the user criterion
- for the mechanical problem criterion, we use the convergence rate of the norm of internal forces (See Eq. 4). That is to say:
$$\frac{|\mathcal{F}_i - \mathcal{F}_{i-1}|^2}{|\mathcal{F}_0|^2} \geq \epsilon_{mech} \quad \text{with, } \mathcal{F} = \sum_{t=1}^{N_t} \left[\hat{\underline{B}}\right]^{\mathrm{T}} [w]^{\mathrm{T}} \left\{\hat{\underline{\sigma}}^t\right\} \tag{21}$$

Regarding the Weighing matrix two options will be compared in this paper.

$\mathcal{H}_0$: $\left[p^t\right] = \mathbf{I}_2, \forall t \in [1, N_t]$,

$\mathcal{H}_1$: numerically computed from stress identification error maps ($\forall e$ and t) using a numerical twin

Table 1 summarizes the inputs, outputs, parameters and assumptions needed for the proposed Data-Driven Identification method. It emphasis the fact that, evenif *DDI* presents itself as a model-free technique for fields of stress tensors identification, part of the modelling framework is hidden in the choice of the constitutive space. Nevertheless, while the framework is constrained the exact form of the constitutive equation remains free. Moreover, the role of user parameters remains significant and many aspects has still to be investigated. This paper will focus on the weighing $[p]$ matrix to help the technique to spread within the experimental mechanics community. The three main output of the method are useful in different ways: (1) the value of the converged *DDI* distance Ψ gives information about local and global quality of the stress solution. Indeed, if the scattering remains high the distance will be high emphasizing either issues with input noise, user parameters or dimensionality of the constitutive space. A proper analysis of this distance may help to improve the constitutive space. Indeed, if relevant dimensions are not taken into account, e.g. temperature in a test where an external heat source imposes very high thermal gradients, it will lead to a significant scattering of the data within the chosen subspace. (2) Mechanical points allows for probing locally (time and space) the mechanical response, for instance in vicinity of crack tip, allowing to access mechanical response in never-seen loading conditions but remain as for DIC, potentially noisy. (3) Material states average the mechanical response and sample, within the constitutive space, an underlying constitutive equation. This quantity could eventually be used to identify a parametric form of a constitutive equations.

Inputs	Outputs	Parameters	Assumptions
$\left[u_{\mathrm{dic}}\right], \{F\}$	$[S]$	$\mathbb{C}_o$	Plane stress
$[B]$	$[\hat{\boldsymbol{\sigma}}]$	N^*	Small strain
$\left[\boldsymbol{\sigma}_{\mathrm{fe}}\right]$	$\{\boldsymbol{\epsilon}^*\}, \{\boldsymbol{\epsilon}^{**}\}$	$\epsilon_{mat}, \epsilon_{mech}$	Constitutive space
	$\{\sigma^*\}, \{\sigma^{**}\}$	$[p]$	
	Ψ		

TABLE 1 Summary of the inputs, outputs, parameters and the assumptions needed for the Data-Driven Identification method proposed in this work. In this table, Ψ gives the *DDI* distance at convergence.

3 | EXPERIMENTAL METHOD

The *DDI* method has been presented and detailed previously. In this section, the experiment investigated will be presented. It consists in a high-speed tensile test performed on a metal sheet with a specific geometry.

3.1 | Specimen material

The material chosen for this experimental campaign is the rate-dependent, low-carbon mild-steel XES (French standards). Its chemical composition is presented in Tab. 2. The quasi-static and dynamic behaviour of this material are relatively well-known. Indeed, for example in the mid 90s, methodologies

were developed allowing to perform double-shear experiments on thin metal sheet in both quasi-static and high strain-rate conditions with highly homogeneous stress and strain states [12]. These methodologies were used to study the shear behaviour of the XES steel – in particular the evolution of the rate sensitivity, for strain-rates ranging from $1\times10^{-3}\,s^{-1}$ to $1\times10^{3}\,s^{-1}$ [18]. The tensile behaviour of this steel has also been investigated. For this purpose, Haugou and its collaborators [13] developed a tensile testing device for split Hopkinson bars. This device allows for non-direct tensile tests to be performed on metal sheets. The configuration was used to characterize the mild-steel for plastic strain-rates between $180\,s^{-1}$ and $440\,s^{-1}$. At last, more recently, some researchers focused on the modelling of spot weld for this material. For instance, using experiments based on Arcan principle, Langrand *et al.* [20, 21] were able to model and characterize the joint when submitted to pure and mixed tensile/shear loads in both quasi-static and dynamic conditions. In 2016, Markiewicz *et al.* [27] went one step further and investigated the behaviour of the material when heat affected by spot welding. Furthermore, the authors studied the strain-rate dependency of the heat affected material and identified parameters (see Tab. 3) for modified Krupkowsky model [31], which is a visco-plastic model (rate-dependent hardening flow model) describing the material. This model is written as:

$$\sigma_{KR} = K X^{a} \left(\varepsilon_0 X^{b} + \varepsilon_p\right)^{nX^{c}}, \quad \text{with } X = \frac{\dot{\varepsilon}_p}{\dot{\varepsilon}_0}, \tag{22}$$

where K, a, b, c, n, ε_0 and $\dot{\varepsilon}_0$ are the model parameters to be identified.

It is inspired from the the Krupkowski hardening flow model (also named Swift hardening model) [], widely used in FEM software, itself inspired from the Hollomon (or Ludwig) hardening flow model [], both used to model quasi-static mechanical responses in plastic regime. Notice that, at the limit of zero strain-rate, modified Krupkowsky model tends to its peer. It translates the complex relationship between plastic yield, hardening and strain-rate that a more simple model, e.g. Johnson-Cook, can not capture. Fig. 2 shows the mechanical response of XES for various strain-rates with the fitter model.

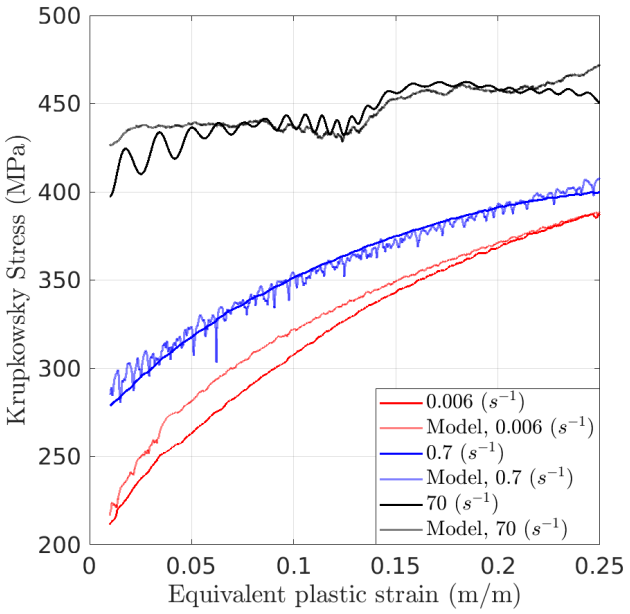

FIGURE 2 Reference data and modified Krupkowsky model previsions from [27].

3.2 | Specimen geometry

The chosen specimen geometry is derived from the one classically used when using a hydraulic tensile test machine (see the next section for more details). Indeed, the use of such a device limits the specimen length and width. In addition, since the *DDI* method relies on the load recorded by the load cell, the sample needs to be symmetrical in the tensile test direction in order to avoid the introduction of any bias in the load measurement (*e.g.* transverse loading).

The main features of the geometry are two symmetrical notches and a central hole (see Fig. 3). Such features are expected to lead to strain concentration bands between the notches and the central hole as well as secondary bands from the central hole to the edge of the sample with an angle of approximately 45°. Hence, the use of such a geometry during one high speed tensile test allows to capture the material's response for wider ranges of strains and strain-rates compared to the standard geometry as well as creates heterogeneous stress-strain states within the specimen.

The specimens were were cut from a 0.8 mm-thick metal sheet in the rolling direction.

3.3 | Experimental setup

The tests conducted in this work are high speed tensile tests. They are conducted using a hydraulic tensile test machine (MTS-819, 20 kN). On this machine, the upper grip is mounted on a modified Hopkinson bar, similarly to the device from [22]. This bar is made of steel (42CD4 rectified) and is instrumented with strain gauges in order to act like a load cell (see Figure 4). In addition, the lower grip is mounted on a sliding bar. The sliding bar is in an enclosing case linked to the actuator. The sliding bar, through the control of the "free fall" length, allows the actuator to reach the imposed displacement speed before loading the sample. The maximum actuator velocity allowing an accurate load measurement, *i.e.* $5\,m\,s^{-1}$, is used for this

C	S	N	Mn	P	Si	Al	Ni	Cr
0.0268	0.0175	0.006	0.202	0.007	0.007	0.07	0.018	0.036
Cu	Mo	Sn	Nb	V	Ti	B	Ca	
0.014	0.002	0.004	0.001	0.002	0.002	≤ 0.0003	≤ 0.0003	

TABLE 2 XES chemical composition (in wt%), data from [27].

Parameters	K (MPa)	ε_0	n	$\dot{\varepsilon}_0$ (s^{-1})	a	b	c
[27]	526.6	0.024	0.221	0.085	0.002	0.385	0.002

TABLE 3 Parameters for the modified Krupkowsky model from [27].

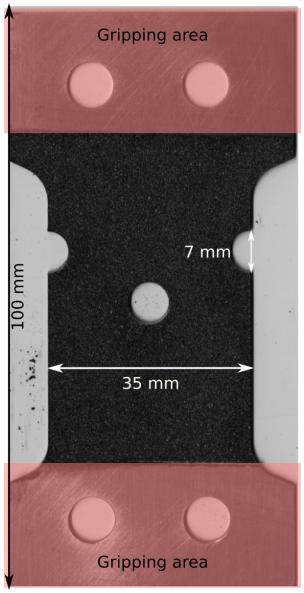

FIGURE 3 Photography of an experimental sample, its principal features are two symmetrical notches and a central hole.

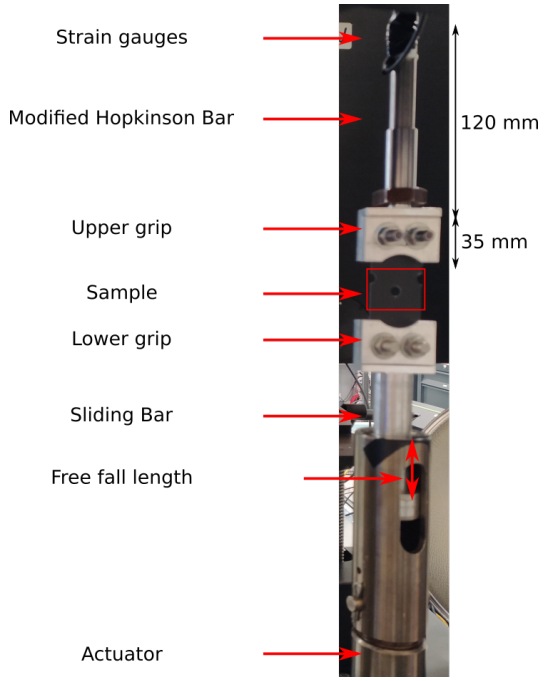

FIGURE 4 Close-up view of the high speed tensile machine setup.

experiment. The "free fall" distance was accordingly set to 25 mm.

3.4 | Imaging setup

The camera used in this work is a Cordin-580. It is a rotating mirror camera that captures 78 images of 8 megapixels (2472 x 3296 pixels) up to 4 million fps. This camera and its specificities have been studied in depth in [37]. For the experiment presented in this work, the camera is equipped with a 90 mm Tamron objective, and records at 68 kfps with a CDS gain of -3 dB (Correlated double sampling) and a CCD gain of 15 % (amplification factor in the analog-to-digital converter)). At such speed, the film duration is about 1.18 ms. In order to provide enough light, two Pro-10 (2400 J each at 10-stops) Xenon flashes from Profoto are used. They are set in normal mode, at 10 f-stops. In that configuration, the illumination typically lasts 2.4 ms with a stable and optimal plateau of 1.1 ms. The flashes and the camera are triggered separately in this experiment. The flashes are triggered using an infrared light-gate system (SPX1189 series Honeywell). It is placed in such manner that it is obscured by the enclosing case. The optical gate will then send a 5 V TTL signal when the enclosing case is at a given distance to the contact with the sliding bar. This distance has to take into account the speed of the actuator as well as the rising time of the flashes (150 µs). It has been empirically determined and set at 3.7 mm from the contact point. The Cordin-580 is triggered using the load cell. When the load reaches a chosen threshold (in this study 6231.5 N, $\approx$ half of the plastic yield), a trigger is sent to the camera.

Upon receiving the trigger, the camera will record the following images, as well as the ones taken up to 100 µs before (this is named post-triggering). These parameters were determined empirically through preliminary tests. Furthermore, the working distance between this camera and the sample is about 31 cm, leading to a pixel size of 14.49 µm. These information are summarized in Tab. 4.

An infrared camera (a Telops M3K) is also used to record the other face of the sample during the experiment (see Fig. 5). The infrared results fall out of the scope of the presented work. Nevertheless, thermal information confirmed that no strong thermomechanical couplings are induced by the strain. Indeed, mean sample temperature rises up to 5 °C while temperature within localization band does not exceed 50 °C before fracture onset. It confirms that the constitutive space used to identify stresses does not have to take into account explicitly temperature (see Sec. 2).

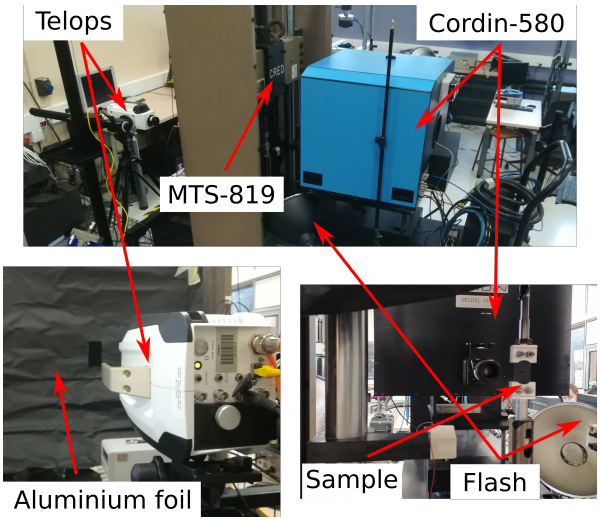

FIGURE 5 Experimental setup for a high speed tensile test, recorded using a visible-light camera and an infrared one.

3.5 | DIC setup and parameters

In order to be able to perform DIC on the images recorded by the camera a reference image is needed [37]. In this work, this image is obtained by recording the black and white paint speckle pattern on the sample using a high definition camera (50M pix, Prosilica GT from Stemmer) combined with the same objective lens as the one used with the Cordin-580, prior to the test. Furthermore, following this methodology, 12 calibration shots were taken with the Cordin camera when the first sample was mounted, prior to the test. These calibration shots are used in order to create a representative model of the distortions induced by the camera in experimental conditions (lens, working distance, magnification, frame rate). Then, in order to correct the eventual rigid body motion between one experiment and the other, a single calibration shot is performed before each of the other experiments.

Camera	Cordin-580
Image resolution	2472 pixels × 3296 pixels
Dynamic Range, Detector	12 bits
Dynamic Range, Image	16 bits
Acquisition Rate	68 kfps
Lens	Tamron SP 90 mm Di Macro
Aperture	f/2.8
Field of view	35.8 mm × 47.8 mm
Image scale	1 pixel = 14.49 µm
Stand-off distance	31 cm
Patterning Technique	Black and White paint

TABLE 4 DIC hardware parameters.

In this work, a continuous mesh is used. Since it is known that strain localization appears in 2 principal bands, the mesh is refined along these bands and in the vicinity of the notches and the hole as well. The element size is 32 pixels on average, but finer along the crack (about 26 pix). A Tikhonov regularization of the DIC problem of 4 elements is used to filter-out spatial noise. The displacements are firstly pointwise convolved with a rolling temporal Savitzky-Golay filtering window of second order with a window size equal to 23 frames (see Tab. 5). Then strain-rates are obtained from strains using a simple 1^{st} order finite difference scheme. Such data filtering marginally affects strain, but significantly decreases the amount of noise on strain-rates.

3.6 | Technical issues and solutions

Due to the complexity of the experiments conducted, some technical issues have to be tackled. This is the aim of this section.

DIC Software	Ufreckles [32]
Shape Function	linear FE triangle elements
Matching Criterion	element-wise ZNSSD
Image Filtering	sensor flattening (vignetting)
Data Processing	U : Tikhonov regularization over 4 elements
Data Post-Processing	$\dot{\epsilon}$: Savitzky–Golay filter of order 2 applied onto U (win = 23 fr)

TABLE 5 DIC analysis parameters.

Load measurement

The load is captured by the load cell during the experiment. However, it has to be adjusted time-wise: indeed, the load is measured by strain gauges while the information is needed on the mesh boundary, in particular for the DDI (see Sec. 2). Hence, due to the distance between the mesh boundary and the strain gauges, a delay has to be taken into account. Figure 4 presents the experimental apparatus, with in particular the distances of interest: the distance between the strain gage and the grip (120 mm using the constructor's data) as well as the distance between the grip and the ROI (≈ 35 mm measured manually). Then, using the modified bar's properties ($E = 205$ GPa and $\rho = 7850\,\mathrm{kg/m^3}$), the delay is computed as follows: $\tau = \frac{\sqrt{\rho}}{\sqrt{E}}$, which yields a delay of 30 µs. This is in the order of magnitude of two Cordin interframes for this experiment. Furthermore, note that even an error of 1 cm in the distance between the grip and the ROI leads to an error of 2 µs for τ, which is negligible regarding our time resolutions.

Pre-stressed sample

The experimental setup is hyper-static, and as a result, the sample when fixed is already pre-constrained. Indeed, the griping device relies on two metallic rods on each side of the sample to maintain it. However, due to its use, the rods are deformed. As a result the sample may be already slightly deformed when placed, before the experiment. This can be evidenced by looking at the displacement fields obtained for the shot taken when the sample is in place and static. A rigid-body motion identified on the first image is subtracted to these fields in order to account for a possible small rotation between the reference image (taken with another camera in a different set-up) and the Cordin images. Figure 6 depicts the averaged over time of the axial and transverse displacement fields with the rigid-body motion subtracted as well as the averaged over time Von-Mises norm of the total strain. This figure shows that the sample is under vertical tension on the right-hand side, as well as horizontal tension on the bottom. Nevertheless, the amplitude of these tensions are about $\pm$ 1 pixels. Furthermore, the averaged over time Von-Mises norm of the total strain clearly shows that the sample is slightly deformed (less than $3\,\mathrm{mm\,m^{-1}}$), which is in the same order of magnitude as the strain measurement uncertainty. Hence, the sample may be pre-constrained by the experimental setup, nevertheless this phenomenon is not significant.

4 | NUMERICAL TWIN

In order to investigate the Data-Driven Identification method introduced in 2 and the influence of the user parameters, especially the weighing matrix $[p]$, a numerical validation is conducted and is presented in this Section. Note that, contrary to classical 1D loading cases, the presented work relies on data existing in a 13 dimension space (3 for $\boldsymbol{\varepsilon}$, 3 for $\dot{\boldsymbol{\varepsilon}}$, 3 for $\boldsymbol{\sigma}$, 3 for $\dot{\boldsymbol{\sigma}}$) ~~, even 14 if we consider the temperature T~~. Such high dimensionality requires developing new ways to display results. Nevertheless, such developments go beyond the scope of this work. Hence, for the sake of simplicity the majority of the results will be presented in sub-spaces using invariant based norms (*e.g.* I_1, Von-Mises). Note that this is not a requirement but just a graphic choice. Any other mechanical norms could have been chosen.

4.1 | Creation of a Numerical twin

The Virtual Image Deformation (VID) is a process that consists in making a numerical twin of an experiment. The use of such a numerical twin allows to have access to a realistic estimation of the data that will be measured during the real experiment. Furthermore, it allows to qualify an experiment in terms of measurability of the fields of interest (in the present case the stress tensors), and their uncertainties. It can also validate an identification procedure and its robustness with respect to realistic experimental conditions. In order for this procedure to be relevant, VID must take into account, as much as possible and as accurately as possible, experimental errors and uncertainties such as:

- The spatial resolution of the imaging system and the DIC sampling, which affects the ability to capture strain gradients,
- The temporal resolution of the imaging system, which affects the temporal derivatives (speed, acceleration),
- In our particular case, when using the Cordin, the bias induced by the camera's distortions which lead to low but still non-negligible displacement uncertainties,
- Sensor noise, which affects the optical flow conservation in DIC and thus displacement uncertainties as well as time derivatives.

Obviously such procedure is never perfect, for instance, it is difficult to take into account strong speckle transformation or even degradation in highly deformed regions during large strains [38], light variation, out-of-plane motions... For these reasons, the use of VID is becoming more and more systematic in the validation of an experimental procedure and of inverse identification procedure [34, 1, 33, 14, 2, 35, 9, 28, 8].

Thus, in the following paragraphs, this construction is described. Several Finite-Elements simulations will be performed using Abaqus with the implicit solver using CPS3T elements. In all the FE simulations the thermomechanical

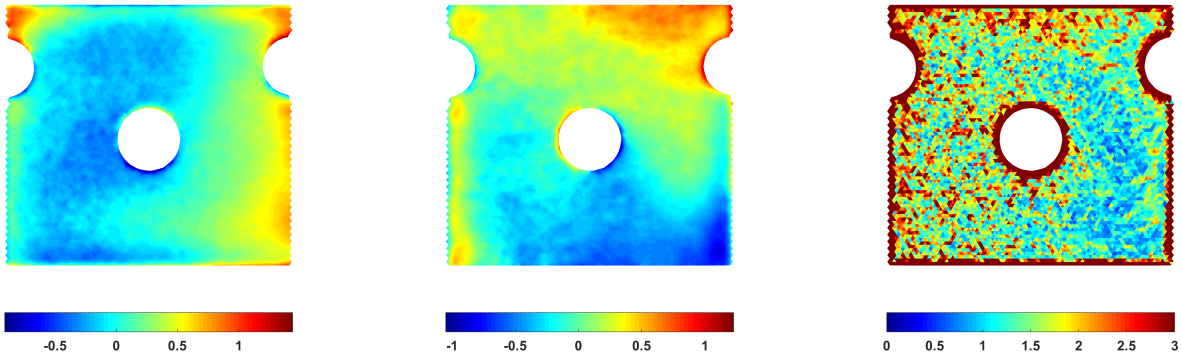

(a) Time average U_x (pix), **(b)** Time average U_y (pix), **(c)** Time average $||\varepsilon_t||_{VM}$ (mm/m),

FIGURE 6 Averaged over time displacement fields and Von-Mises norm of the total strain when the sample is placed in the gripping device and static (1 pixel = 14.5 µm).

Johnson-Cook model will be used as it is implemented by default in FE solvers. Particular attention is given to the influence of the initial solution used in DDI, especially since the Johonson-Cook model is not able to fully capture the complex strain-rate dependency of the material that will be investigated.

Creation of a reference solution (U^{ref}, σ^{ref}, F_y^{ref})

A FE simulation is first performed in order to create a reference solution, which will serve 2 purposes : (1) the construction of Virtual images, (2) to compare the results after using the whole chain leading to the estimation of stress tensors (DIC + DDI).

This simulation is conducted using the model parameters given in in Tab. 7 (this will be called Model A in the rest of this work). They are identified using a tensile test at an average strain-rate of 70 s^{-1} from a previous study [27]. To mimic the experiments, the simulation is performed under imposed displacements on the upper and lower boundaries. On the upper boundary a 0 displacement fields is imposed in both the axial and transverse directions as it is gripped. On the lower boundary, a displacement corresponding to a velocity of 5 $m\,s^{-1}$ is imposed in the axial direction. For simplicity purposes, this simulation is performed using an experimental DIC mesh that was used for the actual experiment (see Fig. 28b). The same mesh will be used throughout the whole procedure.

The outputs of this simulation – namely the displacement fields U^{ref}, the stress fields $\boldsymbol{\sigma}^{\text{ref}}$ and the vertical net force on the upper boundary F_y^{ref} – will be used as references for what follows.

Virtual image deformation

In order to be able to perform DIC on the synthetic images, a texture needs to be applied. For this study a classical black and white paints speckle pattern is considered. The undistorted reference image is thus created using a high resolution camera to record a speckle pattern made with black and white paints. This reference image is then binned down to the Cordin image size. Then, using the same mesh as FE simulation, this image is cropped resulting in the image in Figure 7a. The field of view (cm x cm, see Table 6) matches the aspect ratio of the camera for a pixel size of µm (*i.e.* a magnification of).

Once the reference image created, using the mesh and the displacement fields from the reference simulation, the image is deformed (see Fig. 7b for an example). This is done by performing a loop on the elements of the deformed mesh. For each element, the pixels contained in it are known. Using shape functions and inverse mapping, their position in the undeformed picture is obtained. Their associated grey values can then be retrieved by performing a spatial bi-cubic spline interpolation of the grey value of the reference image. This process is summarized in Figure 8.

Furthermore, in order to be as representative of a real experiment as possible, measurement bias introduced by the distortion variability from one shot to another has to be taken into account. For simplicity purpose, two sets of distortion parameters obtained experimentally are used. The first one (obtained for a specific calibration shot) is used to deform the images and the second one (which is from the statistical distortion model associated to the first set of parameters) is used to perform DIC. As a result, this allows to introduce the right order of magnitude of uncertainty in displacement measurement inherent to the method. Using the composition relationship between the effective displacement u_{simu} and the first distortion field u_d, the imposed displacement u_{virtual} used to deform the images is computed as follows:

$$u_{\text{virtual}}(\underline{X}) = u_{\text{simu}}(\underline{X}) + u_d(\underline{X} + u_{\text{simu}}(\underline{X})). \tag{23}$$

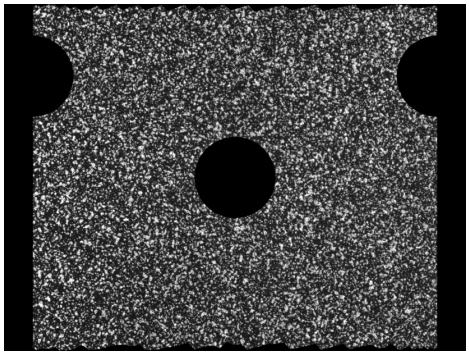

(a) Reference image created synthetically,

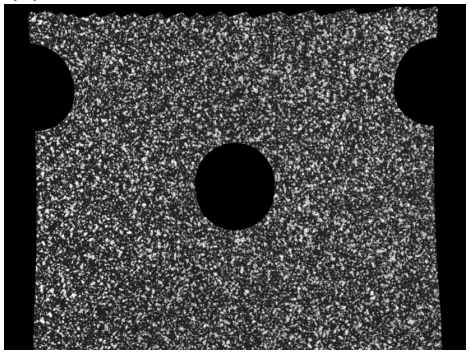

(b) Deformed and distorted image,

FIGURE 7 Example of the reference image and a deformed and distorted image created synthetically.

FIGURE 8 Schematic of the deformation procedure of a synthetic image for one triangular element. The black squares depict the pixels positions in the deformed configuration, while the grey squares depict the pixels positions in the reference one. The red crosses denote the pixels from the deformed configuration projected by an inverse mapping in the reference one. The deformed image for the element is obtained by interpolating the grey levels from the grey squares onto the crosses.

Finally, a realistic noise is added to the deformed and distorted synthetic images. The estimation of grey level noise, meaning apparent grey level variation of one material points from one image to another over time, has been estimated as follows:

- Images of a static reference shot of the sample are deformed back to the undistorted configuration using identified distortion parameters. At that stage, each pixel sees the same material point over time.

- The grey level standard deviation over time of every pixel is computed and its normalized value (by the pixel's grey level) plotted as a function of the mean grey level value of the considered pixel. The plot is presented in Figure 9. This database can be fit with a polynomial P to get the trend of the apparent noise of the camera over its dynamic. The polynomial used is depicted in the figure by the black line.

- This result is used to add random noise to images proportional to pixel grey levels following this equation:

$$\text{noise}(F, p) = F(p) \cdot P(F(p)) \cdot \text{randn}(p), \qquad (24)$$

where $\text{noise}(F, p)$ is the noise that will be added to the pixel p of image F, $P(F(p))$ is the noise value fit by the polynomial for the grey value $F(p)$ and randn is a normally distributed random numbers matrix of the size of F.

At the first order, the polynomial fit shows that the apparent noise converges toward 5 % in the whites, reaches 10 % at about 12 bits (4000) then ramps up to 30 % in the blacks. Notice that, in practice, data presented in Figure 9 is not strictly speaking a noise. Indeed, pixel time variations are in our case not only due to CCD dark noise but to the offset and gain mismatch from one sensor to another, the focus mismatch, as well as the uncertainty on distortion estimation which does not allow for perfectly stabilizing images ($\pm$ 0.1 pixel). This is why we name it apparent noise. In addition, it explains why values are very high compared to mono-sensor ultra-high speed camera (*e.g.* in the order of 1 % of 16 bits for the Shimadzu HPV-X). Nevertheless, apparent noise will affects the optical flow conservation in a similar way to real noise and will have a strong impact on time derivatives.

As a summary, at this stage we have to produced, references kinematic fields as well as images that mimic the response of our imaging system. Applying the dedicated DIC procedure for the Cordin camera allows for capturing realistic displacement fields U^{DIC}. In the next section, the DDI method will be investigated using these fields in order to assess its accuracy as well as the influence of user parameters.

4.2 | Creation of a statically admissible initial solution using a "wrong" model

The creation of an initial guess for the stress field that will be used as an input for the DDI algorithm requires two

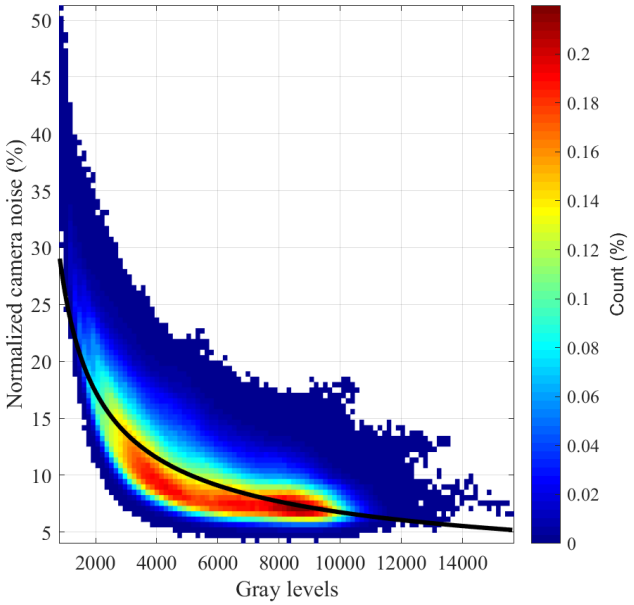

FIGURE 9 Normalized apparent camera noise (in %) versus the mean grey level. The colour denotes the counts (in %), while the black line denotes the polynomials used to model the camera noise.

DIC Software	Ufreckles [32]
Image size	2472 x 3296 pixels
Field of view	cm x cm
Cordin pixel size	5.5 µm
Image scale	1 pixel = µm (Magnification of)
Mesh size	≈ 21 pixels
Data Processing	U: Tikhonov regularization over 4 elements

TABLE 6 Virtual DIC parameters.

consecutive Finite-Element simulations. To validate the DDI procedure, an initialization reasonably far from the solution is chosen. To this effect, the same model as the reference one is chosen but the constitutive parameters are significantly modified. Hence, the initial yield is decreased, whereas the hardening modulus is increased. In addition, to investigate the ability of the DDI to accurately retrieve the strain-rate dependency, the strain-rate dependency is set close to zero. The exact parameters are given in Tab. 7 (it will be called Model B).

- The first simulation is conducted under imposed displacements, using U^{DIC}. The load profile on the upper boundary is extracted from this simulation. This profile is then rescaled in such a manner that, in the end, the net force on the upper boundary is equal to the reference net force F_y^{ref}. The role of this first simulation is to get a nice estimation of the load distribution at the upper bound of the sample.

- The second simulation is then performed under mixed boundary conditions: imposed displacements on the lower boundary, imposed displacements in the X direction and imposed rescaled vertical distribution of forces on the upper bound. This simulation allows to obtain statically admissible stresses $\boldsymbol{\sigma}^{\text{false}}$.

The whole procedure is summarized in Figure 10. In what follows the DDI will be given the total strains $\boldsymbol{\varepsilon}_t^{\text{DIC}}$ (computed from U^{DIC}) and $\boldsymbol{\sigma}^{\text{false}}$ as inputs. This case allows to assess the influence of the measurement errors on the estimation of the stress fields. Hence, the final errors are representative of the ones performed during an experiment. In addition, for comparison purposes, the plastic strains $\boldsymbol{\varepsilon}_p^{DDI}$ associated to the stresses $\boldsymbol{\sigma}^{DDI}$ are computed from the total strains $\boldsymbol{\varepsilon}_t^{DDI}$ using Hooke law, the plastic incompressibility and the small strain assumption: $\boldsymbol{\varepsilon}_p^{DDI} = \boldsymbol{\varepsilon}_t^{DDI} - \mathbb{C}^{-1} : \boldsymbol{\sigma}^{DDI}$.

4.3 | Results and discussions

The DDI is used using 50 time steps using simulation results as described previously.

4.3.1 | Noise-free procedure

For this procedure, the reference displacement fields and the stress fields obtained using Model B are used as inputs for the DDI method. Usually, when using experimental fields for the DDI, the resulting strain fields are smoothed using a median filter with a characteristic length between 2 to 6 elements. In this study, since the experimental displacement fields are regularized using a filter over 4 elements to obtain strain fields in Section 28b, the median filter will have a length of 4 elements.

$[p] = \mathbf{I}_2$

Let us first consider the stresses obtained when using the DDI, and using the identity matrix as weights, and compare them to the reference ones. For this purpose, Figure 11 depicts these stresses in a sub space of the constitutive space built using the Von-Mises norm: $(\|\boldsymbol{\varepsilon}_p\|_{VM}, \|\boldsymbol{\sigma}\|_{VM})$. The reference solution is depicted by the red crosses, while the solution from the DDI is represented by the coloured dots. The colour and the size of the dots are related to the size of the associated material state cluster. First, one can observe that the biggest clusters are associated to mechanical states under elasticity. This is expected considering the fact that plasticity mainly occurs in the bands and after a certain loading step. Hence, most of the sample is under elasticity or very small plastic strains during most of the

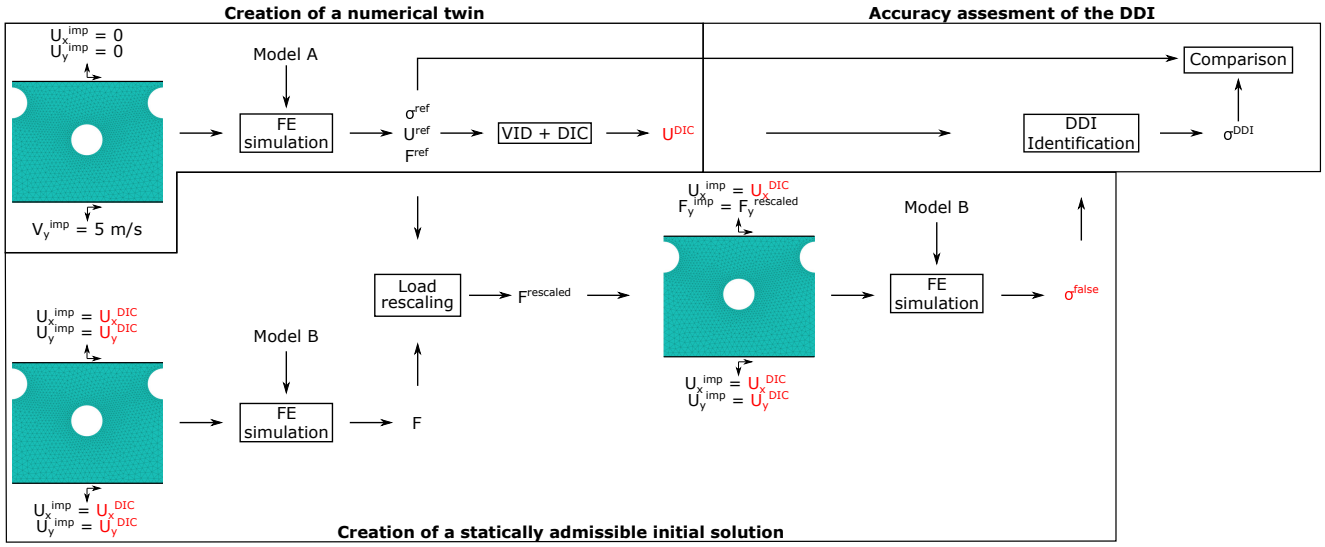

FIGURE 10 Schematic of the numerical test case procedure. In red are the inputs of the DDI algorithm.

	A (MPa)	B (MPa)	n	C	$\dot{\varepsilon}_0$ (s^{-1})	m	T_o (K)	T_{melt} (K)
Model A	394 MPa	136 MPa	0.471	0.0259	69.86 s^{-1}	1.11	300	1350
Model B	315 MPa	272 MPa	0.6123	2.56×10^{-4}	69.86 s^{-1}	1.11	300	1350

TABLE 7 Parameters of the two Johnson-Cook model used for the FE simulations to investigate the DDI algorithm.

experiment time. Furthermore, the fit between the DDI solution and the reference seems to be acceptable for strains up to 0.5, a small deviation is observed beyond these strains.

Figures 12a and 12b depict the evolution temporal of respectively the stress systematic error and the random error. These figures show both the absolute and the relative values, for the initial stress fields (using Model B) and the DDI ones (using $[p] = \mathbf{I}_2$). These figures clearly highlight the effectiveness of the DDI method, which is more pronounced for the systematic error. Indeed, the systematic error is reduced from about 60 MPa (respectively 15 %) to 45 (respectively 12 %), while the random error is reduced from about 48 MPa (respectively 12.02 %) to 44 (respectively 11.3 %). Thus, apart from elasticity (*i.e.* after the first 30 µs), the DDI method is able to estimate the stress fields with a relative accuracy of $12.02\,\%^{\pm 11.3\,\%}$ when using noisefree data.

After considering the temporal evolution of stress errors, it is also of interest to consider their spatial distributions. For this purpose, figures 13a, 13b, 13c and 13d depict the relative temporal systematic and random errors for each element of the geometry, for respectively the initial stress fields (obtained when using Model B) and the ones obtained after the DDI. The first two cartographies show that the initial error is mainly located near the mesh boundaries, as well as where the sample is not submitted to high plastic strains. The initial error is also important near the central hole and notches, where the strain-rate reaches high values. On the other hand, the improvement of the solution by the DDI algorithm is clearly highlighted when one considers the error cartographies of the DDI solutions. Indeed, the errors are lower in most of the elements. The remaining errors are located on the edges of the sample: where the mesh is coarser. Hence, it is expected that the use of a finer mesh may help to improve the results. Furthermore, it is important to note that the error also remain important just below the central holes: where the plastic strain remain low. Incidentally it is also where the sample is in compression.

Construction of a filtering operator

Figures 13c and 13d highlight the fact that some spatio-temporal elements lead to higher stress errors than others. Hence, the use of the identity matrix as weight in the DDI gives the same weight to these elements than those leading to lower stress uncertainties. Another route is to attribute a weight $[p]_{e,t}$ varying continuously for each spatio-temporal element considering their stress uncertainty obtained with the numerical test case. This strategy will thus naturally give less weight to elements leading to high stress uncertainties in the DDI. Thus, the stress estimations obtained should be more robust and more accurate. In a way, such an approach would be very similar to some VFM versions where virtual fields are automatically selected to filter-out noise (optimized Virtual Fields). Here, the

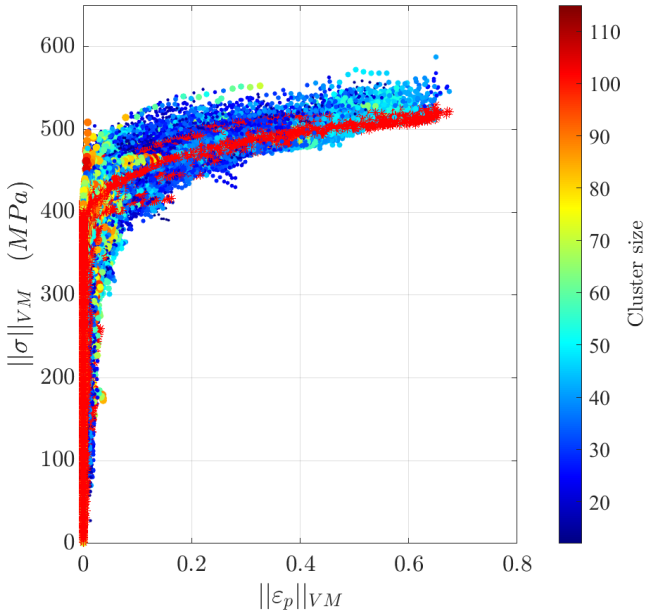

FIGURE 11 Comparison of the DDI output versus the reference solution (in red) in the constitutive space ($\|\boldsymbol{\varepsilon}_p\|_{VM}$, $\|\boldsymbol{\sigma}\|_{VM}$). The marker size and colour for the DDI output are related to the size of the cluster containing the mechanical state.

complexity and non-linearity of the problem does not allow to have an analytical solution, but the use of a numerical twin can produce such a filter.

In this work the weights will be based on the DDI results obtained using the identity matrix. Once these results obtained, for each spatio-temporal element the Von-Mises norm of the stress error is computed. Figure 14 shows the histogram of these errors for all the spatio-temporal elements. The red dashed line denotes the 97$^{\text{th}}$ quantile, *i.e.* 97 % of the errors are comprised between 0 MPa and 140 MPa. Then $[p]_{e,t}$ is computed following the following formula :

$$[p]_{e,t} = \begin{cases} 0.1, & \text{if } ||dS_{e,t}||_{VM} \geq 0.9 \times Q_{97} \\ 1 - \frac{||dS_{e,t}||_{VM}}{Q_{97}}, & \text{otherwise,} \end{cases} \quad (25)$$

where $||dS_{e,t}||_{VM}$ is the Von-Mises norm of the stress error of the element e at t and Q_{97} is the 97$^{\text{th}}$ quantile. A threshold is introduced to avoid elements with negative weights or equal to zero. Thus, the weights vary linearly between 0.1 and 1. At last, in order to have a fair comparison with the other weighting methods, the weights are rescaled so that the sum of all the weights is equal to the number of elements times the number of time steps.

Figure 15 shows the $[p]$ matrix evolution for different time steps. As expected, during the experiment the elements located near the border or the edges of the mesh are discriminated against. In addition, it shows that the elements that are considered reliable are located near the bands: where the plastic strain is more important (*i.e.* where the noise to signal ratio is favorable).

DDI results using the filtering operator

The DDI results obtained using the weighting matrices defined will now be presented. For comparison purposes, Figures 16a, and 16b depict the stress systematic and random error evolutions. These constructed matrices reduce slightly both the relative stress systematic and random errors by about 1 %, leading to the following relative accuracy: 10.69 %$^{\pm 10.48\,\%}$.

4.3.2 | VID procedure

Once the performances of the method assessed using noise-free displacement fields as input, the DDI will now be tested using realistic displacement fields *i.e.* impaired by realistic noise. In the previous subsection, a filtering operator was constructed through the use of weighting matrices. In this subsection, the DDI results using the identity matrix and the said operator will be presented and compared. Then the overall accuracy of the method will be discussed.

Similarly to Figure 11, Figure 17a depicts stresses in the ($\|\boldsymbol{\varepsilon}_p\|_{VM}$, $\|\boldsymbol{\sigma}\|_{VM}$) space. The use of displacement fields impaired with realistic noise introduces a larger spread in the DDI stresses. This phenomenon is particularly significant in the elastic part of the strain-stress curve. To further analyse this observation, Figure 17b depicts the stress relative error for the mechanical states as a function of the Von-Mises norm of the plastic strain. The red points represent the mechanical states under a compressive state ($I_1 \leq 0$) while the blue ones are under a tensile state ($I_1 \geq 0$). This figure shows that the DDI yields relative errors below 15 % when the material's elasto-plastic transition is passed and when the plastic strains remain below 0.5. This is particularly highlighted by the polynomial fit of order 3 for all the data with a plastic strain above 0.01 (the red line in the figure). The grey area represents one standard deviation of the error made by the fit. Let us note that most of the mechanical states under compression remain below a plastic strain of 0.005, *i.e.* in elasticity which explains why they are badly estimated by the DDI. Furthermore, Figures 18a and 18b show despite the introduction of noise in the displacement fields, the accuracy remain similar and is stable. Indeed, these figures show that the DDI results are obtained with an accuracy of 13.0 %$^{\pm 12.1\,\%}$.

It is also of interest to consider the DDI relative error distribution in the space of the stress tensor invariants. For this reason, Figure 19a depicts the DDI error in the space I_1 versus $\|\boldsymbol{\sigma}\|_{VM}$. In addition, a few classical stress states are represented by lines on the figure. To complement this figure, Fig. 19b depicts the distribution of the mechanical points in the

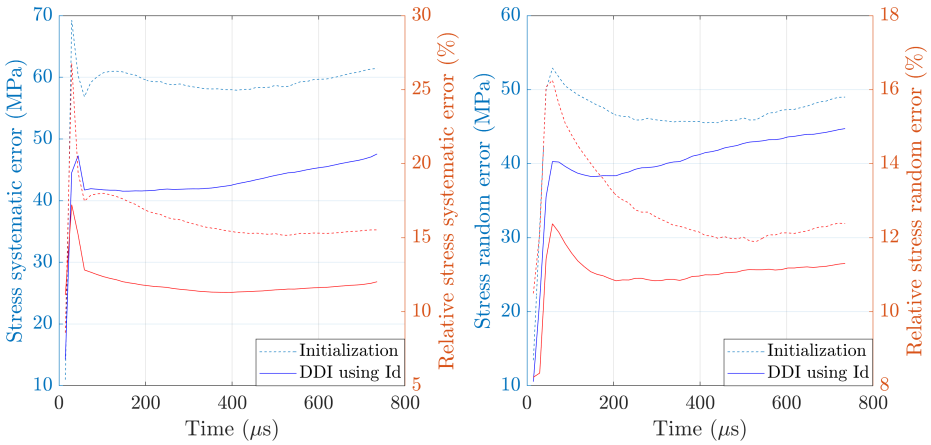

(a) Stress systematic error evolution for the initialization and DDI,

(b) Stress random error evolution for the initialization and DDI,

FIGURE 12 Stress systematic and random error evolution, computed for the initial stress fields and the DDI. Both absolute and relative values are given.

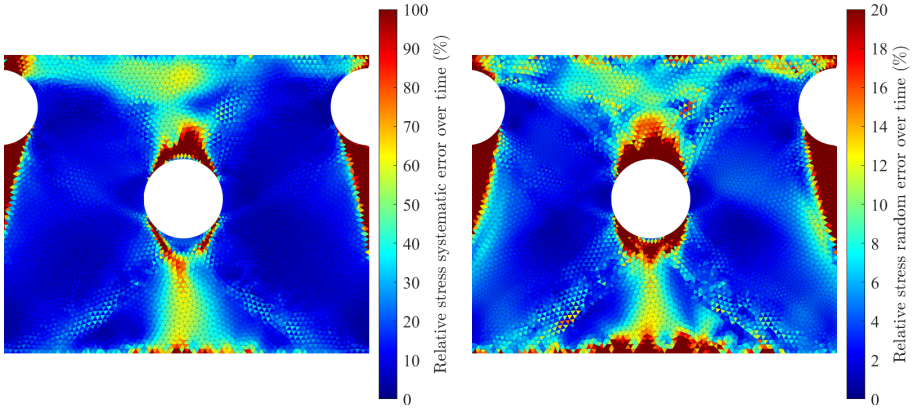

(a) Initialization systematic error (MPa),

(b) Initialization random error (MPa),

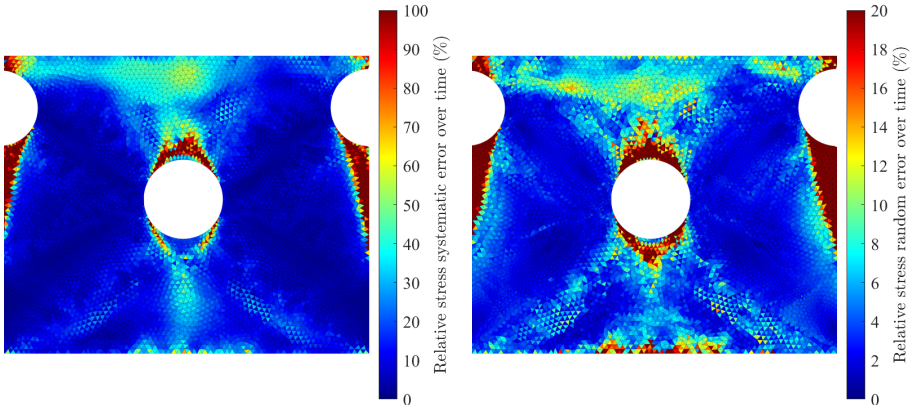

(c) DDI systematic error (MPa),

(d) DDI random error (MPa),

FIGURE 13 Temporal systematic and random errors of each element of the mesh. The errors are computed for the initial stress field as well as for the ones obtained with the DDI.

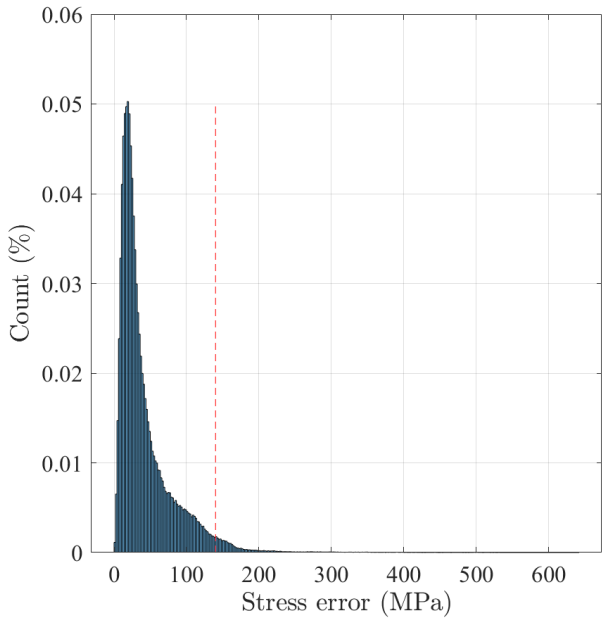

FIGURE 14 Distribution of the stress error Von-Mises norms, for all the spatio-temporal elements. The red dashed line denotes the 97^{th} quantile.

same space. These figures show that the error committed by the method remains relatively low (below 15 %) when redundancy is achieved by the mechanical points (*i.e.* mainly for uniaxial tension states and its vicinity for stresses higher than 200 MPa, and some points in uniaxial compression). On the other hand, when the data available is sparse, the error becomes considerable (higher than 50 %), which is expected.

To further investigate the ability of the DDI method to capture the strain-rate dependency, stress-strain curves can be plotted for different average strain-rates (see Figure 20a). To plot such a figure, the average strain-rate over time for each element is computed. Then, using a clustering algorithm (here k-means), these average strain-rates are regrouped in 10 clusters. The stress-strain curves are then obtained by averaging the stresses and strains for each cluster. Figure 20b then shows the errors at $||\varepsilon_p||_{VM} = 0.01$, 0.05 and 0.1 for the 10 average strain-rates. The circles depict the FE solution using model B, while the stars depict the DDI solution. At last, Figure 20c depicts the relative stress systematic and random error evolutions for each average strain-rates. Figure 20a evidences that a strain-rate sensitivity naturally emerges from the DDI solution. The material hardens more and more with the strain-rate. This is obtained when using the initial guess obtained with model B — which has, as already said, almost no rate sensitivity — as input to the DDI algorithm. This can also be observed on Figure 20b. Indeed, in this figure we retrieve the fact that model A (the reference) and model B have different strain-rate dependencies. This is especially highlighted by the relative error at 5 % and 10 % strain. Indeed, using model B, the error increases with the strain-rate, while the DDI solution remains quasi-constant with an error around 2 %. At last, Figure 20c shows that, apart for very low plastic strains, the DDI errors remain below 15 % for all the average strain-rates considered for plastic strains up to about 0.5. Thus this further confirms the accuracy of $13.0\,\%^{\pm 12.1\,\%}$ previously determined.

To summarize, by using kinematic fields from VID, one can assess the experimental accuracy that can be obtained using the Data-Driven Identification method for our sample geometry, loading conditions and camera. The DDI leads to stress estimations with a relative error of about $13.0\,\%^{\pm 12.1\,\%}$. However, it is able to recover the initial yield stresses and hardening modulus with an accuracy below 5 % for different strain-rates. Furthermore, the inverse identification is most accurate for mechanical states under uniaxial tension, which represent most of the mechanical states using the chosen geometry.

5 | RESULTS AND DISCUSSIONS

update figures and values with new parameters : pe and lc = 2 (computation in progress -> end 03/02/2023)

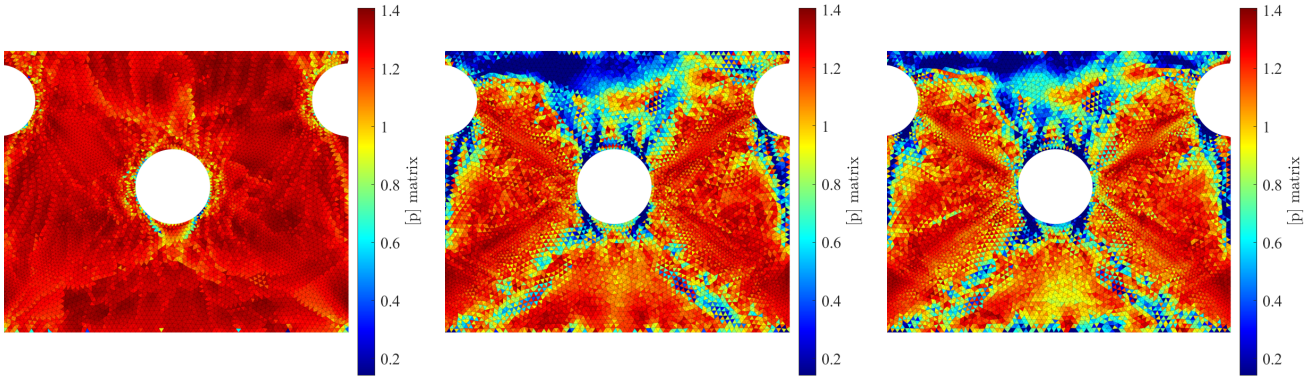

[p] matrix for the first time step [p] matrix for the 25$^{\text{th}}$ time step [p] matrix for the 50$^{\text{th}}$ time step

FIGURE 15 Evolution of the weighting matrix.

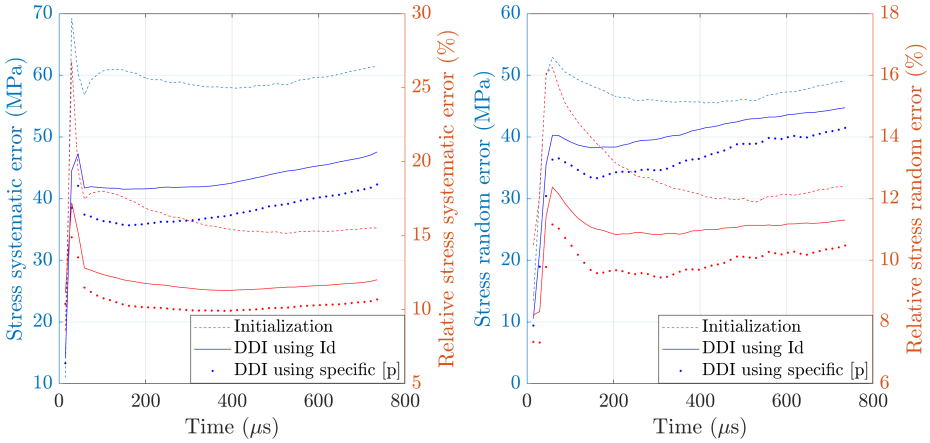

(a) Stress systematic error evolution for the initialization and DDI, **(b)** Stress random error evolution for the initialization and DDI,

FIGURE 16 Stress systematic and random error evolution, computed for the initialization and the DDI when using [p]. Both absolute and relative values are given.

5.1 | Evolution of macroscopic quantities during the test

The deconvolution between the distortions and the effective displacements is made using the camera model built using the 12 calibration shots. In addition, using the reference shot taken prior to the test, the changes of the extrinsic parameters can be taken into account. Finally, the correct pairing between the sensors and the mirror faces is identified using optical considerations ([37]). This allows the displacement, strain and strain-rate fields to be extracted.

Figure 21 depicts the evolution of different quantities of interest during the experiment.

First, let us look at the temporal evolution of the averaged axial displacement and velocity obtained in the whole sample (depicted by the simple lines) and of the nodes located at the bottom of the mesh (depicted by the lines with markers), *i.e.* close to the sample head where the loading is applied. Figure 21a shows displacement in blue and velocity in red. The three vertical dashed lines are the time steps for which associated fields will be discussed later-on. Note that the zero in the timeline correspond to the time when the Cordin-580 is triggered by the load cell, hence the negative times for the first images. The loading of the specimen induces immediately on the loaded edge a displacement ramp, reaching about 2.8 mm before the initiation of the crack. The averaged axial displacement in the whole sample has a similar behaviour, with a lower slope, and reaches about 2 mm. The velocities in the whole

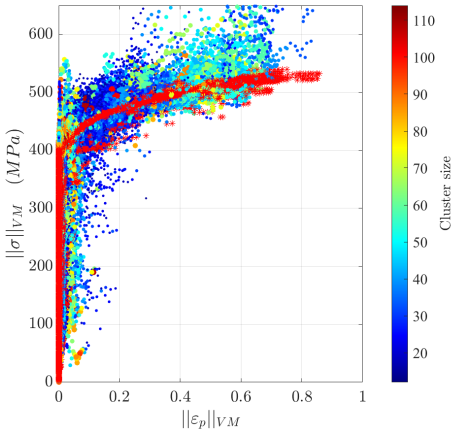

(a) Comparison of the DDI output versus the reference solution (in red) in the constitutive space ($\|\boldsymbol{\varepsilon}_p\|_{VM}$, $\|\boldsymbol{\sigma}\|_{VM}$),

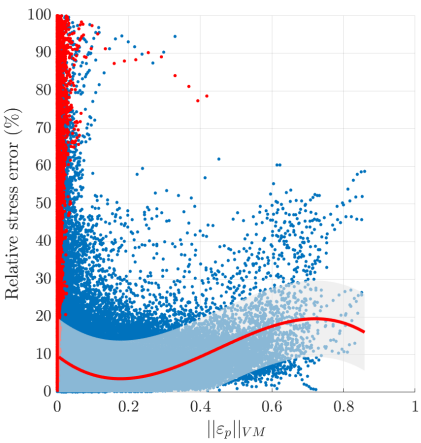

(b) Relative error of the stress estimation in function of $||\varepsilon_p||_{VM}$,

FIGURE 17 Comparison of the DDI ouput versus the reference solution and stress relative error evolution obtained with noisy displacement fields.

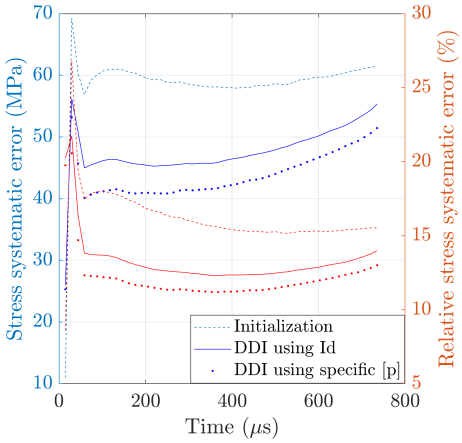

(a) Stress systematic error evolution for the initialization and DDI,

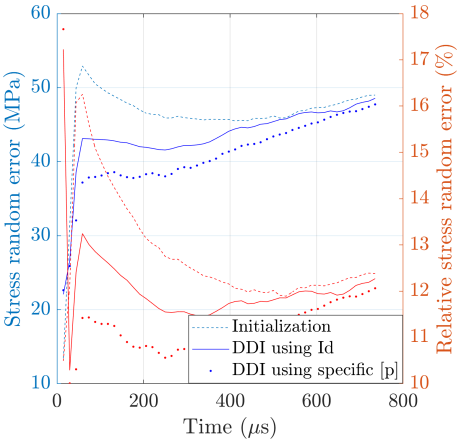

(b) Stress random error evolution for the initialization and DDI,

FIGURE 18 Stress systematic and random error evolution, computed for the initialization and the DDI when using [p]. Both absolute and relative values are given.

sample or for the nodes at the bottom of the mesh have the same trend. The velocities evidence two stages: from the beginning to approximately t = 370 µs the velocities increase in the tension direction, then from t = 370 µs to t = 620 µs they decrease. The second stage can be explained by considering the possibility that the contact between the sliding bar and its enclosing case is not permanent. Indeed, if the sample goes faster than the actuator, then when there is no more contact its speed will naturally decrease until there is contact again. One way to verify this hypothesis would have been to record accurately the speed of the actuator (using DIC with a high speed camera for instance). However, this was not done for these experiments. During the experiment, the maximum speed reached on the loaded edge is about 4.8 m s^{-1} in about 476 µs which represent an acceleration on the order of 1×10^4 m s^{-2}; while the maximum speed experienced by the whole sample is about 3.5 m s^{-1}.

Figure 21b plots the evolution of the Von-Mises norm of both the total strain (in blue) and total strain-rates (in red) either in the whole sample (depicted by the simple lines) or

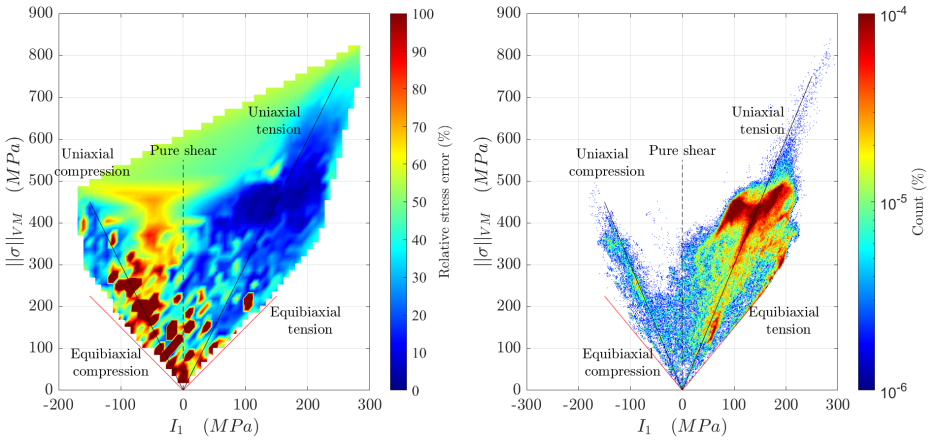

(a) Cartography of the relative error in $(I_1, \|\boldsymbol{\sigma}\|_{VM})$,

(b) Distribution of the mechanical points in $(I_1, \|\boldsymbol{\sigma}\|_{VM})$,

FIGURE 19 Relative stress error and distribution of the mechanical points in the stress invariant space $(I_1, \|\boldsymbol{\sigma}\|_{VM})$.

in a localization band during the experiment (depicted by the lines with markers). This figure shows that during the first 100 µs of the experiment, the sample is mainly in an elastic regime ($||\varepsilon_t||_{VM} \leq 0.005$). Furthermore, the total strain in the localization band goes past 0.01 after about 150 µs, after which it increases following a ramp until about 0.22 before the crack initiation. On the other hand, the global total strain reaches only 0.05 before the crack initiation, which shows that deformation mainly occurs in the localization bands. In the considered band, two stages of the normalized total strain-rate can be observed. First, it ramps up to 375 s^{-1} in about 300 µs. Then, the normalized total strain-rate reaches a plateau and oscillates between 350 s^{-1} and 400 s^{-1}. Similarly to the total strain, the total strain-rate in the whole sample is lower than the one observed in the bands as it reaches only 100 s^{-1}.

At last, Figure 21c shows the evolution of the load during the experiment (in blue). It also depicts – for information purpose only – the average temperature increase (in red) either in the whole sample (depicted by the simple line) or in the considered band (depicted by the line with markers). Two stages can be evidenced for the load. During the first 150 µs the load ramps up until 8 kN. Then it reaches a plateau and oscillates around 8.5 kN. Considering an initial cross section S_0 equal to 1.68×10^{-5} m^2 (subtracting the holes), the engineering stress can be estimated at 500 MPa. This value is in line with the ones obtained in [13]. A slight increase of temperature of about 0.3 °C is observed while the sample should slightly cool down by the same amount due to thermoelasticity. This observation is explained by the fact that the dedicated calibration procedure applied to retrieve temperature fields is not is not reproducible enough to entirely get ride of small variations, and thus does not allow to capture thermoelasticity. However, note that thermoelasticity would have been almost impossible to capture anyway when considering the measurement uncertainty achieved with the procedure used (300 mK), which is already in the same order of magnitude as thermoelastic effects. Nevertheless, after 100 µs, the temperature increases follow the same trend as the normalized total strains, as expected. The sample temperature increase reaches 15 °C on average in the localization band before crack initiation with a rate on the order of 25 K/ms. On the other hand, the temperature increase in the whole sample reaches about 4 °C before crack initiation.

5.2 | Displacement ans strain fields

Figure 22 shows sample images, displacement fields in both directions, the axial strain fields for the three time steps introduced previously. The displacement fields obtained are consistent with a tensile test. The first two images underline the fact that the tensile test is not perfectly axial. Indeed, the axial displacements are higher on the left-hand side of the sample. This phenomenon was observed for all the experiments performed as well as on the preliminary tests. In turn, crack initiation systematically begins on the left-hand side of the sample before the right-hand side. No clear explanations have been found for this observation. It may partly due to the fact that the sample is already pre-constrained, and a non-planar contact between the sliding bar and its enclosing case may also come into play. However, no clear evidences have been found to confirm these hypotheses. The strain fields at 246.79 µs further confirm the fact that the load imposed on the sample is not symmetrical since strains are higher in the left band. The sample geometry

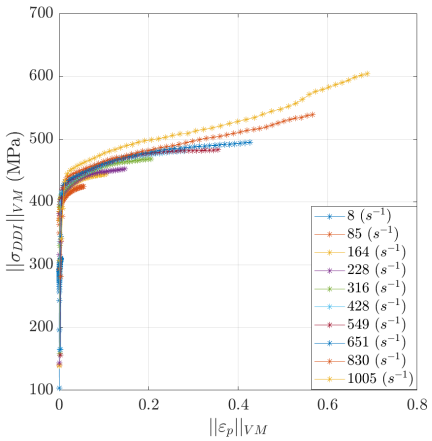

(a) Stress-strain curves for different averaged strain-rates obtained in one experiment,

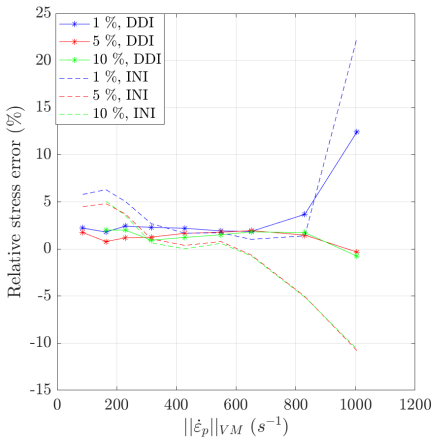

(b) Relative stress error evolution with the strain-rate, computed at different strains, using the DDI solution or FE solution,

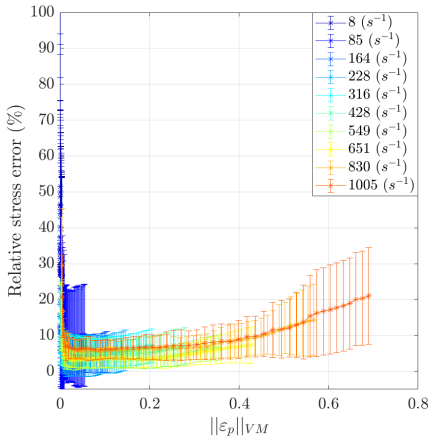

(c) Relative stress error evolution for the different averaged strain-rates,

FIGURE 20 Assessment of the DDI impact on stress-strain curves for different averaged strain-rates.

induces localization bands as predicted by the FE simulations with little strain everywhere else.

In addition, plastic strain and plastic strain-rate ranges experienced by the sample during the test is investigated. To this effect, Figure 23 depicts the plastic strain *versus* plastic strain-rate occurrences that are observed through the chosen ROI during the whole test. White areas represent states that the sample never reached. Since the material considered has a plastic strain of fracture between 0.26 and 0.3 [4], the x-axis is limited to a plastic strain of 0.35. This figure shows that most of the sample during the experiment undergoes small plastic strain as well as small plastic strain-rates. This is consistent with the strain fields obtained. Furthermore, let us note that before cracking, only a few points reach a total strain higher than 0.25. The strain and strain-rates in the range of respectively [0 – 0.25] and [0 s^{-1} – 500 s^{-1}] predicted by the numerical twin are recovered quite nicely.

5.3 | DDI experimental application to the XES characterization campaign

relire et changer figures / valeurs

Stress fields

The DDI algorithm has been presented and then applied to a numerical test case in the previous section. Now the proposed method will be applied to the data obtained during the XES characterization campaign. The performance of the proposed

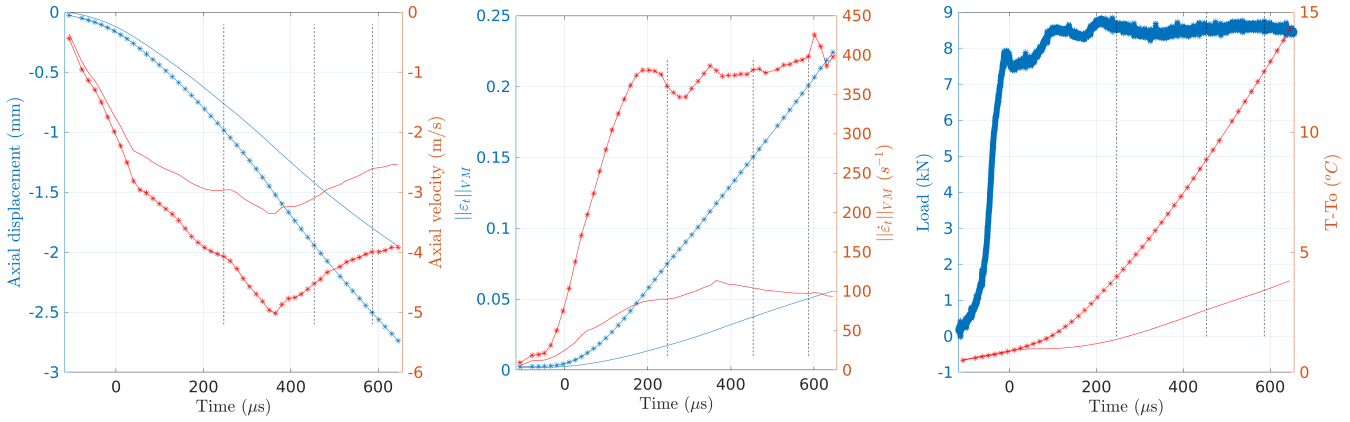

(a) Average U_y and V_y, **(b)** Average total strain and strain-rates, **(c)** Average temperature raise and load,

FIGURE 21 Evolution of different quantities of interest during an heterogeneous test. A simple line denotes the evolution of the considered quantity averaged in the whole sample, while a line with marker denotes its evolution in a particular zone (either the bottom of the mesh or the localization band).

methodology will be discussed as well as the intrinsic limitations of the method, of the material as well as the geometry chosen.

The experimental procedure for the DDI is very similar to the one presented in Fig. 10. In this case, the experimental data replace the ones obtained from the first simulation of the numerical test case. The load that will be used to rescale the load profile is the one captured by the load cell during the dynamic tensile test adjusted following the method presented in Section 3. Furthermore, as the DDI requires two FE simulations to be performed, the material model chosen for the initialization is the Johnson-Cook model and the parameters used are the one identified on the raw data from ONERA (*i.e.* the model A from the numerical test case).

At last, with the numerical twin the consequent contribution of the use of weighting matrices $[p]$ based on the spatio-temporal elements' stress uncertainties, rather than just identity has been demonstrated. Indeed, it is observed that the use of such matrix drastically reduces the mechanical states spread and thus leads to a better sampling of the material's response. Hence, all the results presented are obtained using the constructed weighting matrices.

Once the DDI algorithm applied, the mechanical and material states are available. From these states the Von-Mises norm of the stresses can be obtained. Figure 24 depicts the spatial cartographies of respectively the plastic strains, the Von-Mises stresses as well as the Von-Mises norm of the stress correction performed by the method for the three different time steps. The plastic strains are obtained using Hooke's law, plane stress, plastic incompressibility and the small strain assumption. The elastic properties are identified from the reference data for the XES steel. The cartography of the Von-Mises stresses of the last image (Fig. 24f) shows that, as expected, the notches and the central hole create stress concentration bands. In these bands the Von-Mises stresses reach about 500 MPa. In addition, in the secondary bands, the stress is about 400 MPa. Furthermore, Fig. 24i shows that the DDI deviates from the initial guess the most around the notches and the holes, with substantial corrections since they reach up to 200 MPa. However, since these corrections concern elements of the mesh near a hole, these number should be taken with caution. Indeed, it stands for reason that the experimental kinematic fields are less accurate in these regions, which may in turn have an impact on the stress retrieved with the DDI. In addition, it can be noted that the DDI also applies correction in the upper and lower region of the central hole, similarly to the numerical test case, where the sample is under compression.

Let us recall that the experiment was designed to provide different loading paths of the material and wide spectra of strain and strain-rates during a single test. Hence, Figure 25 enables the verification of these specifications. Fig. 25a depicts the stress distribution in the space $(I_1, \|\boldsymbol{\sigma}\|_{VM})$ for the selected mechanical states. It follows that this figure is an indicator of the stress triaxiality that occurs during the experiment. This figure shows that the sample is mainly under an uniaxial tensile state. However, some compression and shear states are reached within the specimen. In addition, Fig. 25b shows that the strain and strain-rate spectra mainly seen by the specimen are $[0 - 0.21]$ and $[0\,s^{-1} - 500\,s^{-1}]$. Nevertheless, some regions of the sample reach higher strain and higher strain rate values. In order to associate these states to a region in the sample, several

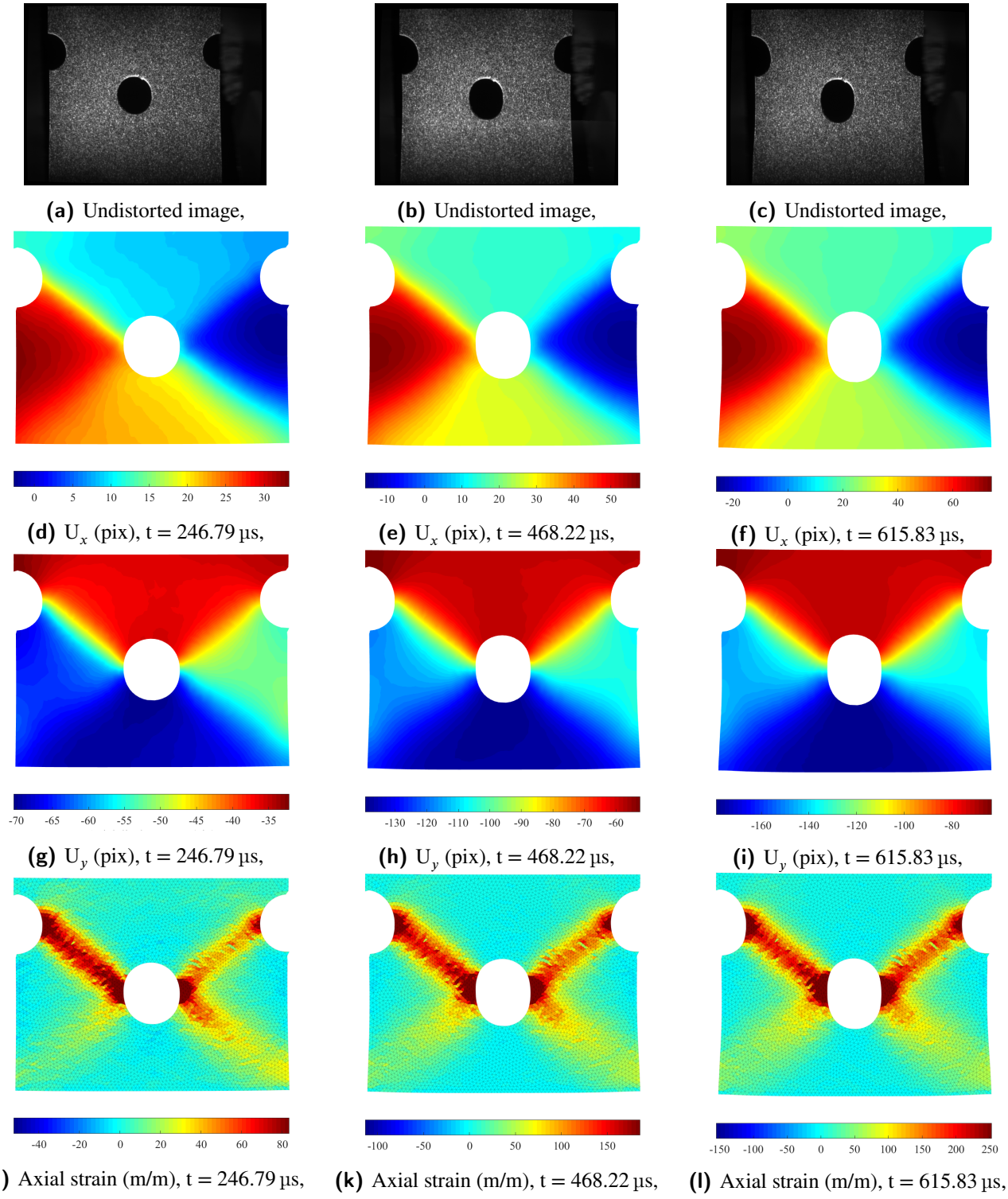

(a) Undistorted image, **(b)** Undistorted image, **(c)** Undistorted image,

(d) U_x (pix), t = 246.79 µs, **(e)** U_x (pix), t = 468.22 µs, **(f)** U_x (pix), t = 615.83 µs,

(g) U_y (pix), t = 246.79 µs, **(h)** U_y (pix), t = 468.22 µs, **(i)** U_y (pix), t = 615.83 µs,

(j) Axial strain (m/m), t = 246.79 µs, **(k)** Axial strain (m/m), t = 468.22 µs, **(l)** Axial strain (m/m), t = 615.83 µs,

FIGURE 22 Undistorted images, displacement fields, strain fields obtained during a dynamic tensile test, for different time steps.

elements located at different regions of interest of the sample are selected (see Fig. 25c). The loading paths of these elements are depicted in the previous figures considered. As it can be expected, the region above and below the hole (and by extension the notches) are under a compressive state. Moreover, as expected the elements in the band are mainly in a uniaxial tensile state. Fig. 25b clearly highlights that the different regions

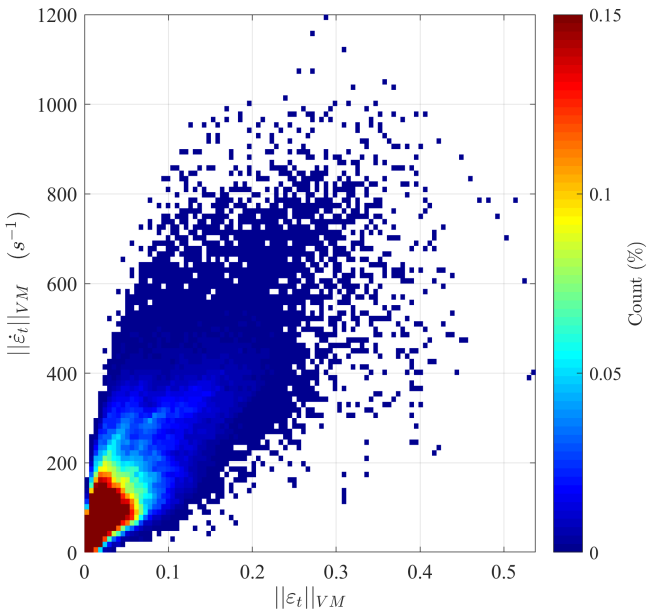

FIGURE 23 Von-Mises norm of the strain vs Von-Mises norm of the strain-rates distribution obtained during the experiment, prior to crack initiation. The colour corresponds to a 2D histogram plot. The count per bin is normalized by the number of element in the ROI multiplied by the number of time steps. The strain states that were never experienced by the sample remain white.

of the bands are under different but quasi-constant strain-rates. This further justifies the specimen geometry since it clearly demonstrates that at least the results of uniaxial tensile tests performed at different strain-rates can be retrieved.

Material behaviour of the XES steel: comparison with the reference data

By construction, the material states best fit the behaviour of the material. Figure 26a depicts projection of the material states. The black and red lines are the raw data from previous characterization of the XES steel performed at ONERA. These figures show that the spreading of the material states is more important on the experimental data than on the numerical test case (see Fig. **??**). Let us also note that even after the selection of the clusters, some material states with singular behaviours are remaining. However, most of the material states remaining are still representative of the behaviour of the material. Indeed, the behaviour of the material at $70\,s^{-1}$ from previous characterization is for instance well captured by the DDI method, in the same range of strain-rate (see the colour). This also confirms the fact that the material considered in this study, known to be strain-rate dependent, has a dependency which fades at about $100\,s^{-1}$. Indeed, the stress response variation from $100\,s^{-1}$ to $500\,s^{-1}$ is more packed than from $1\,s^{-1}$ to $70\,s^{-1}$. Moreover, similarly to Fig. 20a, Figure 26b shows 10 stress-strain curves obtained for different averaged strain-rates, and the reference data are depicted by the dashed lines. The grey area around the dashed line represent a relative uncertainty of $\pm$ 10 %. This figure shows that the data obtained for an average strain-rate of $69\,s^{-1}$ fit remarkably well the reference data at $70\,s^{-1}$. Nevertheless, when taking into account the uncertainty on the stress estimation from Section **??**, the data from $41\,s^{-1}$ to $194\,s^{-1}$ are also in line with the reference data. In particular, the initial yield stresses as well as the hardening modulus obtained at these strain-rates are in line with the reference data. The figure also allows to confirm the fact that the strain-rate dependency fades off around $100\,s^{-1}$, and also confirms a softening of the material response for strains below 0.05 (see Fig. 27a). Furthermore, this figure can be compared to the stress-strain curves obtained in the literature [13], that are recalled in Figure 27. While the DDI stress estimations are in line with our reference data from [27], they differ slightly from the ones in Fig. 27a. Indeed, while we observe (using DDI) a saturation of the yield stress and hardening at about $160\,s^{-1}$ with a stress peak near 500 MPa, data obtained from [13] at $200\,s^{-1}$, $360\,s^{-1}$ and $440\,s^{-1}$ show an increase of the peak stress up to 600 MPa followed by a massive softening. Nevertheless, Fig. 27b highlights the difficulty to have consistent results with different experimental apparatus at high strain-rates. Indeed, by using different techniques, the stress obtained at a plastic strain of 0.1 at a strain-rate of $500\,s^{-1}$ has an uncertainty of about 50 MPa which represent a relative error of about 10 %. Regarding Figure 27b, one sees that our DDI results are closer to data obtained on SHPB or using the special apparatus designed by Haugou [13]. While the question of the reproducibility of the data using different experimental apparatus remains open, Figure 26b shows that DDI and a dedicated sample geometry allows to accurately capture, with a single apparatus, consistent elasto-plastic data from$30\,s^{-1}$ to about $300\,s^{-1}$.

The material states obtained using this DDI method can also be compared to the stresses predicted by the modified Krupkowsky model that better fits the non-linear strain-rate dependency of the XES steel than the Johnson-Cook model. Since neither the material states nor the direct estimation of Krupkowsky stress from experimental strains and strain-rates will verify the equilibrium, the comparison can be considered as fair. Hence, Figure 28 displays three cartographies of the difference between the stresses predicted by Krupkowsky and the material states: the first one is in the $(\|\boldsymbol{\varepsilon}_p\|_{VM}, \|\dot{\boldsymbol{\varepsilon}}_p\|_{VM})$ space with markers to denote the position of the material states. The second one depicts the discrepancy but in the stress invariant space while the last one is the spatial cartography

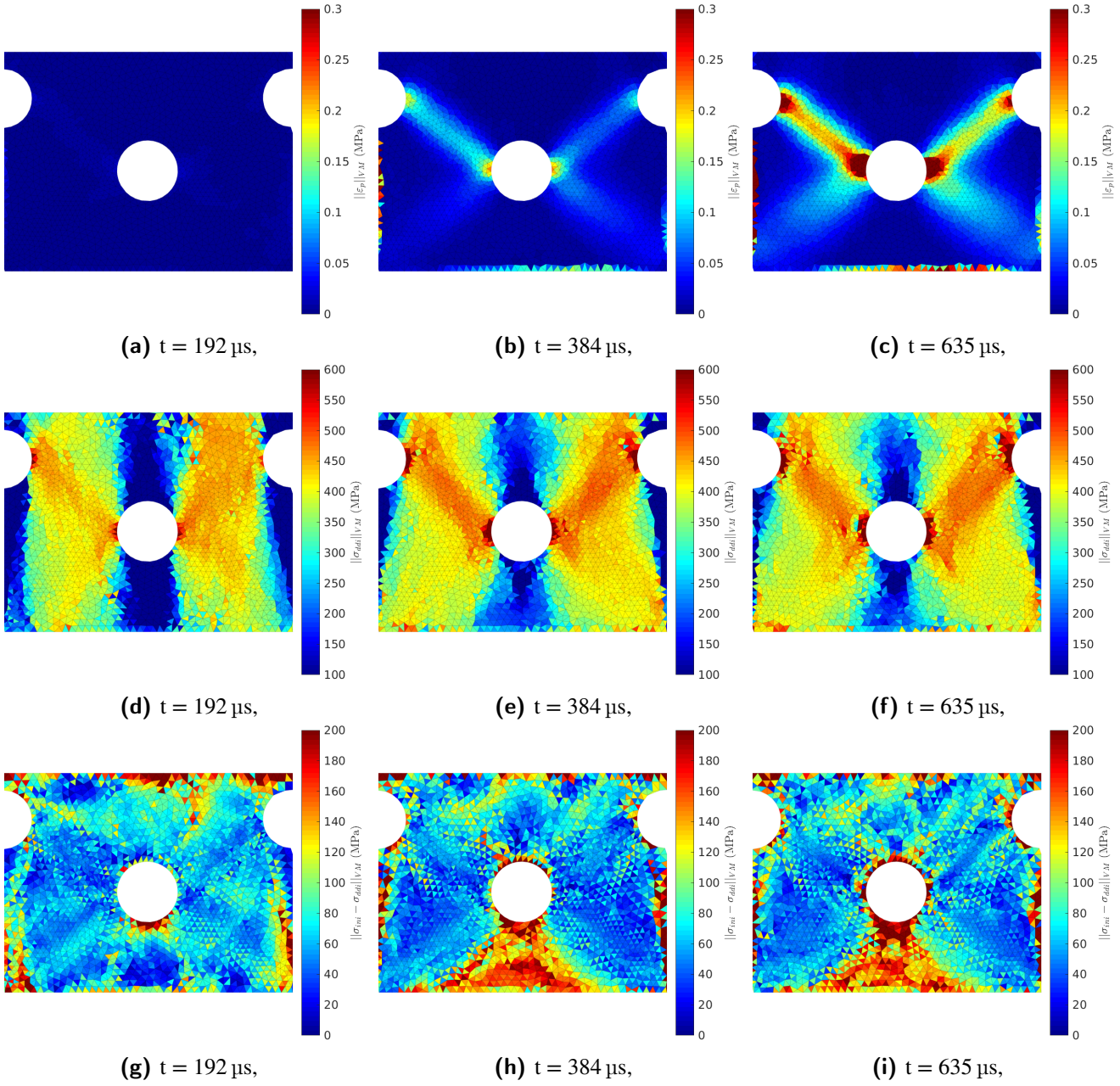

(a) t = 192 µs, **(b)** t = 384 µs, **(c)** t = 635 µs,

(d) t = 192 µs, **(e)** t = 384 µs, **(f)** t = 635 µs,

(g) t = 192 µs, **(h)** t = 384 µs, **(i)** t = 635 µs,

FIGURE 24 Cartographies of the plastic strains, stresses and their corrections performed by the DDI, for three different time steps.

of the discrepancy. Since the modified Krupkowsky model describes the plastic flow, it is not able to predict stresses in elasticity. Hence, the discrepancy cartography in the stress invariant space only holds meaning in plasticity. This is why this cartography is truncated for values of stresses higher than 200 MPa[1]. It can be observed on the first cartography that the stress discrepancies are mainly higher than 10 % in two zones: for low values of strain combined with high values of strain-rates and for a specific horizontal band at a strain-rate of about 250 s^{-1}. As it was shown earlier with Figure. 25, the first zone is mainly experienced by the elements near the hole (*e.g.* the light blue points), and thus the strain-rates and stress values have to be taken with precautions. In addition, this zone is also associated with few clusters of data, which also explains the significant discrepancy. Indeed, Fig. 28a clearly highlights the influence of the cluster distribution on the discrepancy: the more data is available in a region, the

[1] *Nota Bene*: a criterion based on the plastic strain (*e.g.* a threshold at 0.005) would have been more pertinent. However, in our case, some edge effects would remain and thus add non relevant information in the figure.

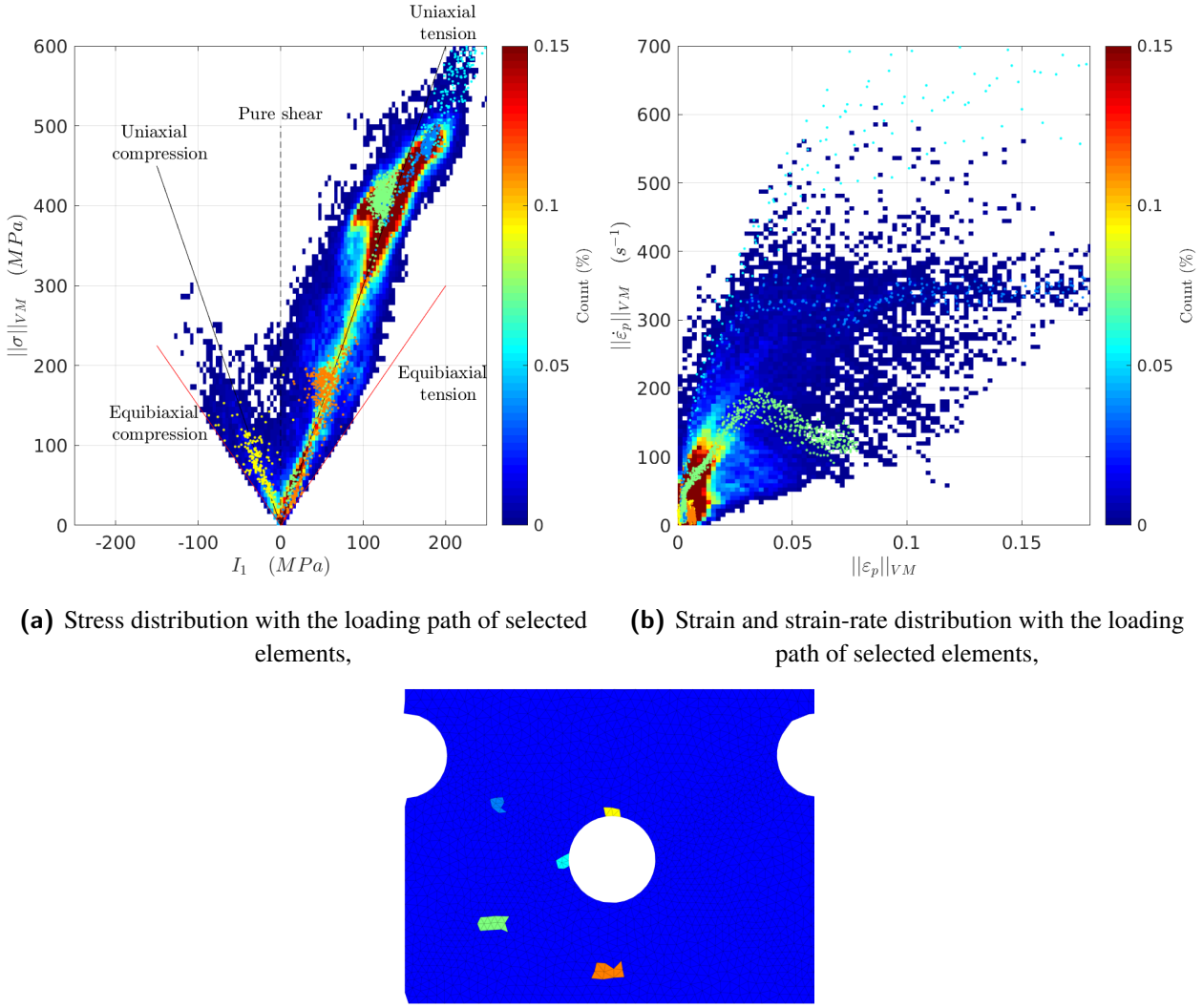

(a) Stress distribution with the loading path of selected elements,

(b) Strain and strain-rate distribution with the loading path of selected elements,

(c) DDI mesh and localization of the selected elements,

FIGURE 25 Stress distribution, strain and strain-rate distributions during the experiment for the selected mechanical states. The loading paths of a few selected elements are superimposed on these distributions.

lower the discrepancy is. However, no clear explanations was found to explain the second zone of significant error located around $250\,\mathrm{s}^{-1}$. Indeed, this zone is described by several material points as illustrated by Fig. 28a. Let us note that apart from the two regions described, the discrepancies remain within the accuracy interval observed for states subjected to uniaxial tension in Section 4 which further comforts the relevance of the DDI stress estimations. Moreover, the spatial cartography shows that the discrepancies are mainly located near the notches and the central hole: where the stresses are estimated less accurately using the chosen geometry. At last, the cartography of the difference between the prediction using the modified Krupkowsky model and the DDI results in the stress invariant space is in quite good agreement with the one obtained in Section 4. Indeed, this figure shows that the DDI method is able to match the predictions from the constitutive model when the material is under uniaxial tension, within a relative discrepancy of about 10 %. All these results comfort the fact that the modified Krupkowsky model, even calibrated over 3 uniaxial curves, is able to extrapolate well at higher strain-rates and when we slightly deviate from its validity loading configuration domain.

Furthermore, the material states obtained with the DDI can be used in a more conventional way to identify constitutive parameters. Parameters are identified using the material states obtained in this work. Since these states do not contain quasi-static data, the quasi-static data from ONERA is also

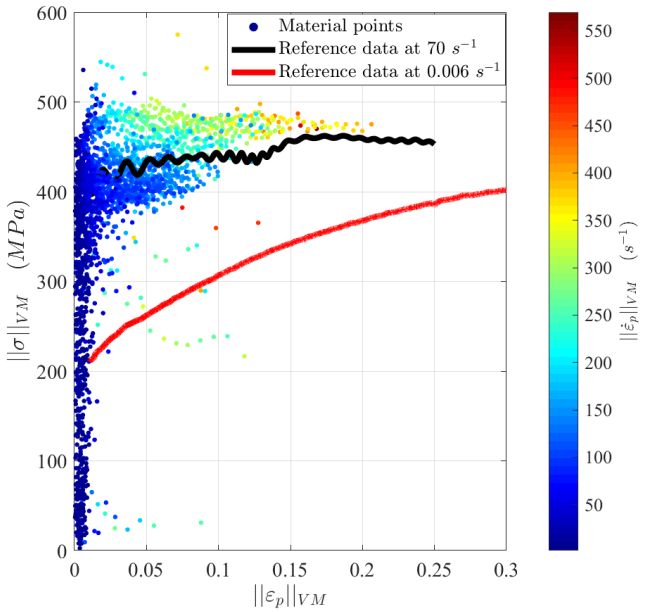

(a) Material states in $(\|\boldsymbol{\varepsilon}_p\|_{VM}, \|\boldsymbol{\sigma}\|_{VM})$. The colour of the markers denote the strain-rates, while the lines denote the reference data from ONERA,

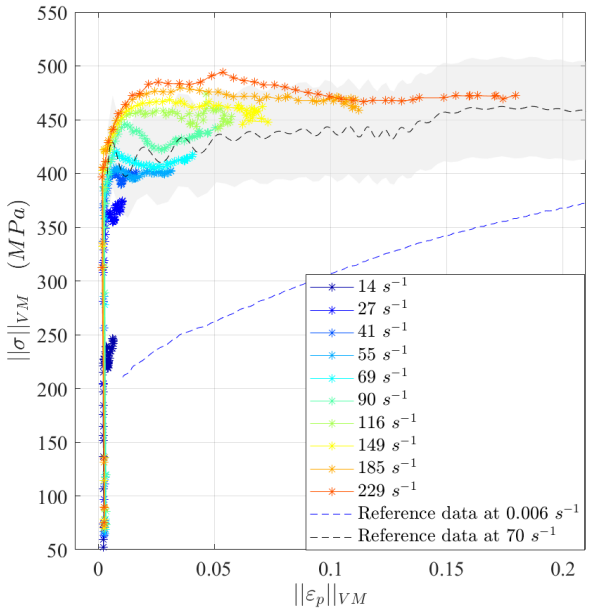

(b) Stress-strain curves for different averaged strain-rates extracted from the selected material states during one experiment,

FIGURE 26 Material states in the space$(\|\boldsymbol{\varepsilon}_p\|_{VM}, \|\boldsymbol{\sigma}\|_{VM})$ as well as stress-strain curves for different averaged strain-rates obtained during one experiment.

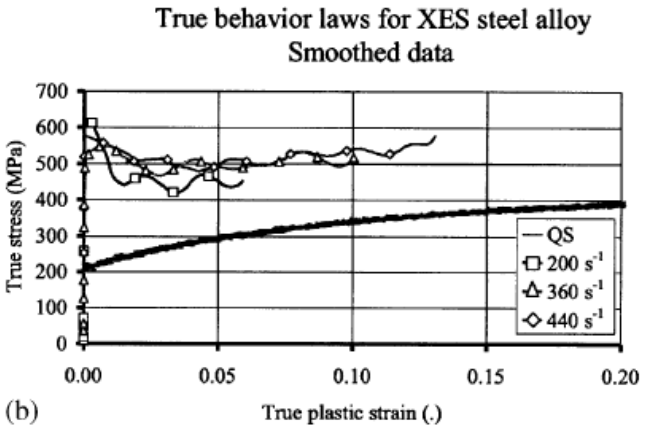

(a) Stress-strain curves obtained for the XES for different strain-rates from [13],

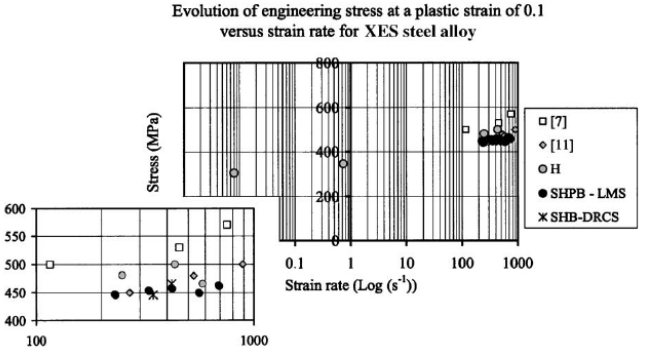

(b) Evolution of the stress at a plastic strain of 0.1 in function of the strain-rate using different techniques, from [13],

FIGURE 27 XES characterization data from [13] and comparison of the results obtained using different experimental techniques.

taken into account, in order to ensure that the parameters identified characterize the material from quasi-statics to high strain-rates. The identification is performed for strains higher than 0.01. The parameters obtained are presented in Tab. 8, which also recall the parameters identified in Section **??**. As in Section **??**, strong variations are observed in particular for exponent c. In addition, ε_0, $\dot{\varepsilon}_0$ and b, which capture the strain-rate dependency, also differ significantly from the reference parameters ($\geq 40\,\%$). Nevertheless, by checking the discrepancies between reference data from ONERA and the modified Krupkowsky model based on the updated parameters using DDI stresses (see Fig 29), one observes that the reference data are capture within 6–7 % of relative error for the quasi-static response and the one at $70\,s^{-1}$. In addition, the data are captured within 10 % for the intermediate response $(0.67\,s^{-1})$. This indicates that the model has a weak sensitivity to its parameters, and also that its 7 parameters can be recovered from only 2 tests: a quasi-static one, and a heterogeneous and

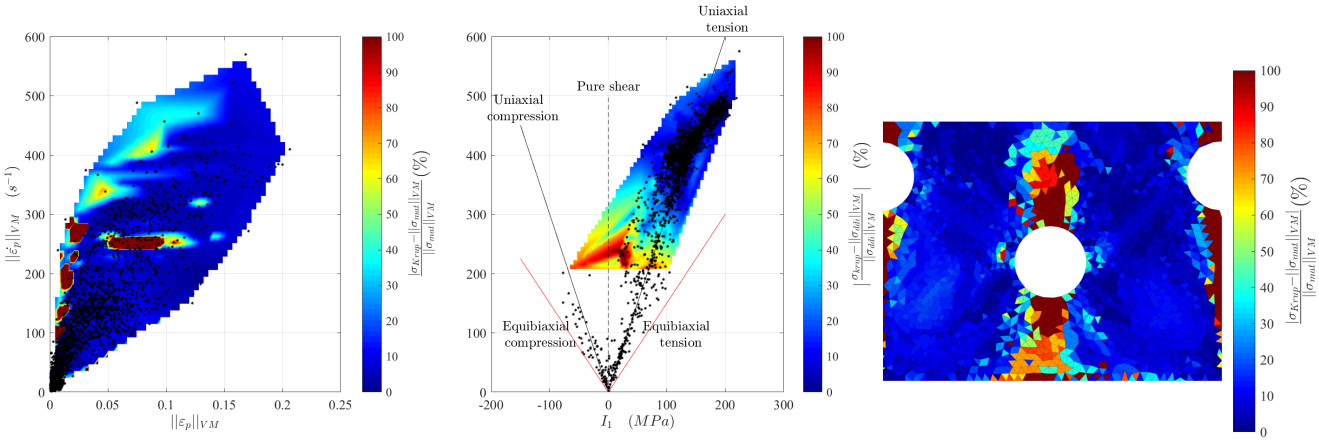

(a) Cartography of the relative error in $(\|\boldsymbol{\varepsilon}_p\|_{VM}, \|\dot{\boldsymbol{\varepsilon}}_p\|_{VM})$, with the cluster distribution superimposed,

(b) Cartography of the relative error in the stress invariant space using material states,

(c) Spatial cartography of the discrepancy between the prediction and the material states at the last image,

FIGURE 28 Comparison between the stress predictions using the modified Krupkowsky model and the material states from the DDI.

high strain-rates one.

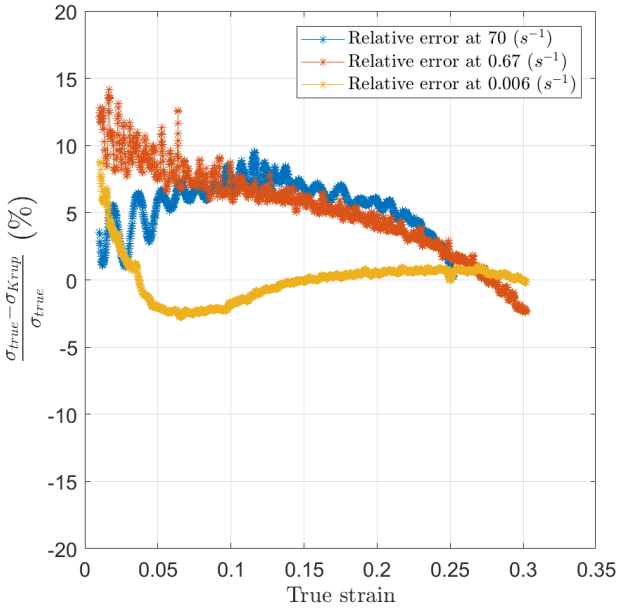

FIGURE 29 Relative errors between the reference data and the fit using the identified parameters.

To summarize, the DDI method has been applied to the experimental data obtained in Part **??**. The stresses have been reconstructed. The stress distribution confirms that the sample is mainly under uniaxial tension during the experiment, but some regions are under compression and shear (the region above and below the hole and notches for instance). The strain and strain-rate spectra that the sample is submitted to are [0 – 0.21] and [0 s^{-1} – 500 s^{-1}]. Furthermore, the DDI algorithm is able to retrieve the behaviour identified during previous characterization campaigns. In particular, using the material states and data from a simple quasi-static test, constitutive parameters can be identified for the modified Krupkowsky model, which allow to retrieve the behaviour with a relative error below 10 % for strain-rates from 0.01 s^{-1} to a few hundreds of s^{-1}. At last but not least, based on the accuracy assessment performed in the previous section and a comparison with the predictions of the modified Krupkowsky model, this model's stress predictions can be considered with confidence even when extrapolated for higher strain-rates than the ones used to calibrate it.

6 | CONCLUSIONS AND PERSPECTIVES

In this paper, the Data-Driven Identification method is presented. Its accuracy has been assessed using a numerical twin. Then, a pre-notched sample with a central hole has been subjected to a high speed tensile test. Fullfield kinematic data have been obtained and quantitatively captured the events during the test. At last, these fullfield kinematic fields have been used as input for the DDI to estimate stress fields during the experiment. The main conclusions are as follows:

Parameters	K (MPa)	ε_0	n	$\dot{\varepsilon}_0$ (s^{-1})	a	b	c
Section **??**	544.5	0.032	0.259	0.06	0.0002	0.328	0.0002
This work + QS data	532.0	0.0133	0.2373	0.1391	0.0002	0.4639	0.0038
Relative variation (%)	2.3 %	58.5 %	8.4 %	−131.8 %	0 %	−41.4 %	−1800 %

TABLE 8 Comparison of the modified Krupkowsky model parameters identified using data from ONERA or from this work combined with quasi-static data from ONERA.

- The parameters of the DDI method play an important role in the stress reconstruction. The analysis performed on the numerical test case lead to the selection of these parameters.

- The numerical test case illustrates the ability of the proposed methodology to retrieve the material behaviour despite the use of a wrong set of constitutive parameters as initialization. It showed in particular that the algorithm is able to retrieve the material's strain-rate dependency accurately.

- The accuracy of the stress field estimations is $10.69\,\%^{\pm 10.48\,\%}$ (relative error). Note that these values are lower bound since the kinematic fields used for the numerical test case are noisefree. Using the results from Virtual Image Deformation, the impact of noise on the stress estimation can be assessed. An accuracy of $13.0\,\%^{\pm 12.1\,\%}$ is obtained on the stress estimation. At last, using the DDI Data to perform identification leads to relative errors lower than 10 %.

- The application of the proposed method to the experimental data allows estimating stress fields. The material behaviour captured by the material states are consistent with the data obtained at ONERA during previous experimental campaigns. In the presented study, the stress are retrieved with confidence for strains and strain-rates in the range of [0.01 – 0.21] and [$10\,s^{-1}$ – $500\,s^{-1}$].

- By combining the data from this work and data from a simple quasi-static test, constitutive parameters can be identified. These parameters are able to correctly retrieve the behaviour of the material over several strain-rates decades, with a relative error that remains below 7 %.

- The comparison with the constitutive model classically used for this material shows that discrepancies are mainly located in the hole and notches vicinity. It also highlights the necessity of having loading paths as rich as possible: the DDI is consistent with the constitutive model for strain and strain-rate spectra where a lot of data is available.

ACKNOWLEDGEMENTS

The support of Région Pays de la Loire, Nantes Métropole and European Union through grant Connect Talent IDS is gratefully acknowledged. The support of ANR through grant ANR-16-CE30-0007-01 is also gratefully acknowledged. Finally the authors would like to acknowledge all the colleagues and PhD students contributing to the informal working group, *OutLaw*, at GeM, especially Adrien Leygue and Raphael Langlois for the fruit-full discussions and their recent developments in rate-dependent DDI.

References

[1] Badaloni, M., M. Rossi, G. Chiappini, P. Lava, and D. Debruyne, 2015: Impact of experimental uncertainties on the identification of mechanical material properties using DIC. *Experimental Mechanics*, **55**, no. 8, 1411–1426, doi:10.1007/s11340-015-0039-8.
URL http://link.springer.com/10.1007/s11340-015-0039-8

[2] Bouda, P., B. Langrand, D. Notta-Cuvier, E. Markiewicz, and F. Pierron, 2019: A computational approach to design new tests for viscoplasticity characterization at high strain-rates. *Computanional Mechanics*, **64**, no. 6, 1639–1654, doi:10.1007/s00466-019-01742-y.
URL http://link.springer.com/10.1007/s00466-019-01742-y

[3] Cameron, B. C. and C. Tasan, 2021: Full-field stress computation from measured deformation fields: A hyperbolic formulation. *Journal of the Mechanics and Physics of Solids*, **147**, 104186, doi:10.1016/j.jmps.2020.104186.
URL https://linkinghub.elsevier.com/retrieve/pii/S0022509620304130

[4] Cherouat, A., H. Borouchaki, and Z. Jie, 2018: Simulation of Sheet Metal Forming Processes Using a Fully Rheological-Damage Constitutive Model Coupling and a Specific 3D Remeshing Method. *Metals*, **8**, no. 12, 991, doi:10.3390/met8120991.
URL http://www.mdpi.com/2075-4701/8/12/991

[5] Dalémat, M., M. Coret, A. Leygue, and E. Verron, 2021: Robustness of the data-driven identification algorithm with incomplete input data, working paper or preprint.
URL https://hal.archives-ouvertes.fr/hal-03028848

[6] Dalémat, M., M. Coret, A. Leygue, and E. Verron, 2019: Measuring stress field without constitutive equation. *Mechanics of Materials*, **136**, 103087, doi:10.1016/j.mechmat.2019.103087.
URL https://linkinghub.elsevier.com/retrieve/pii/S0167663619302376

[7] Eggersmann, R., T. Kirchdoerfer, S. Reese, L. Stainier, and M. Ortiz, 2019: Model-Free Data-Driven inelasticity. *Computer Methods in Applied Mechanics and Engineering*, **350**, 81–99, doi:10.1016/j.cma.2019.02.016.
URL https://linkinghub.elsevier.com/retrieve/pii/S0045782519300878

[8] Fletcher, L., F. Davis, S. Dreuilhe, A. Marek, and F. Pierron, 2021: High strain rate elasto-plasticity identification using the image-based inertial impact (IBII) test part 1: Error quantification. *Strain*, **57**, no. 2, doi:10.1111/str.12375.
URL https://onlinelibrary.wiley.com/doi/10.1111/str.12375

[9] Fletcher, L. and F. Pierron, 2018: An image-based inertial impact (IBII) test for tungsten carbide cermets. *Journal of Dynamic Behavior of Materials*, **4**, no. 4, 481–504.

[10] — 2020: The Image-Based Inertial Release (IBIR) Test: A New High Strain Rate Test for Stiffness Strain-Rate Sensitivity Identification. *Experimental Mechanics*, **60**, no. 4, 493–508, doi:10.1007/s11340-019-00580-6.
URL http://link.springer.com/10.1007/s11340-019-00580-6

[11] Fletcher, L., J. Van-Blitterswyk, and F. Pierron, 2019: A novel image-based inertial impact test (IBII) for the transverse properties of composites at high strain rates. *Journal of Dynamic Behavior of Materials*, **5**, no. 1, 65–92.

[12] Gary, G. and W. K. Nowacki, 1994: Essai de cisaillement plan appliqué à des tôles minces. *Journal de Physique IV*, **04**, no. C8, C8–65–C8–70, doi:10.1051/jp4:1994809.
URL http://www.edpsciences.org/10.1051/jp4:1994809

[13] Haugou, G., E. Markiewicz, and J. Fabis, 2006: On the use of the non direct tensile loading on a classical split Hopkinson bar apparatus dedicated to sheet metal specimen characterisation. *International Journal of Impact Engineering*, **32**, no. 5, 778–798, doi:10.1016/j.ijimpeng.2005.07.015.
URL https://linkinghub.elsevier.com/retrieve/pii/S0734743X05001107

[14] Jones, E., J. Carroll, K. Karlson, S. Kramer, R. Lehoucq, P. Reu, and D. Turner, 2018: Parameter covariance and non-uniqueness in material model calibration using the Virtual Fields Method. *Computational Materials Science*, **152**, 268–290, doi:10.1016/j.commatsci.2018.05.037.
URL https://linkinghub.elsevier.com/retrieve/pii/S0927025618303501

[15] Kirchdoerfer, T. and M. Ortiz, 2016: Data-driven computational mechanics. *Computer Methods in Applied Mechanics and Engineering*, **304**, 81–101, doi:10.1016/j.cma.2016.02.001.
URL https://linkinghub.elsevier.com/retrieve/pii/S0045782516300238

[16] — 2017: Data Driven Computing with noisy material data sets. *Computer Methods in Applied Mechanics and Engineering*, **326**, 622–641, doi:10.1016/j.cma.2017.07.039.
URL https://linkinghub.elsevier.com/retrieve/pii/S0045782517304012

[17] — 2018: Data-driven computing in dynamics: Data-driven computing in dynamics. *International Journal for Numerical Methods in Engineering*, **113**, no. 11, 1697–1710, doi:10.1002/nme.5716.
URL https://onlinelibrary.wiley.com/doi/10.1002/nme.5716

[18] Klepaczko, J. R., H. V. Nguyen, and W. K. Nowacki, 1999: Quasi-static and dynamic shearing of sheet metals. *European Journal of Mechanics - A/Solids*, **18**, no. 2, 271–289, doi:10.1016/S0997-7538(99)80016-3.
URL https://linkinghub.elsevier.com/retrieve/pii/S0997753899800163

[19] Langlois, R., M. Coret, and J. Réthoré, 2022: Non-parametric stress field estimation for history-dependent materials: Application to ductile material exhibiting piobert–lüders localization bands. *Strain*, e12410.

[20] Langrand, B. and A. Combescure, 2004: Non-linear and failure behaviour of spotwelds: a "global" finite element and experiments in pure and mixed modes I/II. *International Journal of Solids and Structures*, **41**, no. 24-25,

6631–6646, doi:10.1016/j.ijsolstr.2004.06.009.
URL https://linkinghub.elsevier.com/retrieve/pii/S0020768304003245

[21] Langrand, B. and E. Markiewicz, 2010: Strain-rate dependence in spot welds: Non-linear behaviour and failure in pure and combined modes I/II. *International Journal of Impact Engineering*, **37**, no. 7, 792–805, doi:10.1016/j.ijimpeng.2010.01.004.
URL https://linkinghub.elsevier.com/retrieve/pii/S0734743X10000163

[22] LeBlanc, M. and D. Lassila, 1996: a hybrid technique for compression testing at intermediate strain rates. *Experimental Techniques*, **20**, no. 5, 21–24, doi:10.1111/j.1747-1567.1996.tb00459.x.
URL http://doi.wiley.com/10.1111/j.1747-1567.1996.tb00459.x

[23] Leygue, A., M. Coret, J. Réthoré, L. Stainier, and E. Verron, 2018: Data-based derivation of material response. *Computer Methods in Applied Mechanics and Engineering*, **331**, 184–196, doi:10.1016/j.cma.2017.11.013.
URL https://linkinghub.elsevier.com/retrieve/pii/S0045782517307156

[24] Leygue, A., R. Seghir, J. Réthoré, M. Coret, E. Verron, and L. Stainier, 2019: Non-parametric material state field extraction from full field measurements. *Computunational Mechanics*, **64**, no. 2, 501–509, doi:10.1007/s00466-019-01725-z.
URL http://link.springer.com/10.1007/s00466-019-01725-z

[25] Liu, C., 2021: Nonuniform Stress Field Determination Based on Deformation Measurement. *Journal of Applied Mechanics*, **88**, no. 7, 071005, doi:10.1115/1.4050535.
URL https://asmedigitalcollection.asme.org/appliedmechanics/article/88/7/071005/1104370/Nonuniform-Stress-Field-Determination-Based-on

[26] MacQueen, J. et al., 1967: Some methods for classification and analysis of multivariate observations. *Proceedings of the fifth Berkeley symposium on mathematical statistics and probability*, Oakland, CA, USA, volume 1, 281–297.

[27] Markiewicz, E., B. Langrand, N. Leconte, J. Fabis, and T. Dupuy, 2016: A methodology for the viscoplastic behaviour characterisation of spot-weld heat affected materials. *Journal of Materials Processing Technology*, **238**, 169–180, doi:10.1016/j.jmatprotec.2016.07.022.
URL https://linkinghub.elsevier.com/retrieve/pii/S0924013616302394

[28] Pierron, F. and L. Fletcher, 2019: Generalized stress–strain curves for IBII tests on isotropic and orthotropic materials. *Journal of Dynamic Behavior of Materials*, **5**, no. 2, 180–193, doi:10.1007/s40870-019-00197-9.
URL http://link.springer.com/10.1007/s40870-019-00197-9

[29] Pierron, F., H. Zhu, and C. Siviour, 2014: Beyond Hopkinson's bar. *Philosophical Transactions of the Royal Society A: Mathematical, Physical and Engineering Sciences*, **372**, no. 2023, 20130195–20130195, doi:10.1098/rsta.2013.0195.

[30] Platzer, A., A. Leygue, L. Stainier, and M. Ortiz, 2021: Finite element solver for data-driven finite strain elasticity. *Computer Methods in Applied Mechanics and Engineering*, **379**, 113756, doi:10.1016/j.cma.2021.113756.
URL https://linkinghub.elsevier.com/retrieve/pii/S004578252100092X

[31] Priadi, D., C. Levaillant, L. Penazzi, E. Di Pasquale, and S. Aita, 1991: Introduction of strain rate effects in constitutive equations suitable for sheet metal stamping applications. *MECAMAT 91*, 1991.

[32] Réthoré, J., 2018: *UFreckles, doi:10.5281/zenodo.1433776*.

[33] Rossi, M., M. Badaloni, P. Lava, D. Debruyne, and F. Pierron, 2016: A procedure for specimen optimization applied to material testing in plasticity with the virtual fields method. *AIP Conference Proceedings*, AIP Publishing LLC, 200016.
URL http://aip.scitation.org/doi/abs/10.1063/1.4963634

[34] Rossi, M., P. Lava, F. Pierron, D. Debruyne, and M. Sasso, 2015: Effect of DIC spatial resolution, noise and interpolation error on identification results with the VFM: Effect of DIC spatial resolution, noise and interpolation on VFM identification. *Strain*, **51**, no. 3, 206–222, doi:10.1111/str.12134.
URL https://onlinelibrary.wiley.com/doi/10.1111/str.12134

[35] Seghir, R. and F. Pierron, 2018: A Novel Image-based Ultrasonic Test to Map Material Mechanical Properties at High Strain-rates. *Experimental Mechanics*, **58**, no. 2, 183–206, doi:10.1007/s11340-017-0329-4.

[36] Stainier, L., A. Leygue, and M. Ortiz, 2019: Model-free data-driven methods in mechanics: material data identification and solvers. *Compututational Mechanics*, **64**, no. 2, 381–393, doi:10.1007/s00466-019-01731-1.

URL http://link.springer.com/10.1007/s00466-019-01731-1

[37] Vinel, A., R. Seghir, J. Berthe, G. Portemont, and J. Réthoré, 2021: Metrological assessment of multi-sensor camera technology for spatially-resolved ultra-high-speed imaging of transient high strain-rate deformation processes. *Strain*, **57**, no. 4, e12381, doi:https://doi.org/10.1111/str.12381.
URL https://onlinelibrary.wiley.com/doi/abs/10.1111/str.12381

[38] Witz, J.-F., P. Lecomte-Grosbras, A. Morch, C. Martel, F. Lesaffre, and M. Brieu, 2017: Digital image correlation for large strain. *International Digital Imaging Correlation Society*, Springer, 163–167.

□